Construction and Building Materials 448 (2024) 138152

Contents lists available at ScienceDirect

Construction and Building Materials

journal homepage: www.elsevier.com/locate/conbuildmat

In and out of plane behaviour of TRM strengthened heritage masonry elements

M. Liapopoulou [a,b], D.V. Bompa [b], A.Y. Elghazouli [a,c,*]

[a] Dept of Civil and Environmental Engineering, Imperial College London, UK
[b] Dept of Civil and Environmental Engineering, University of Surrey, UK
[c] Dept of Civil and Environmental Engineering, Hong Kong Polytechnic University, Hong Kong

ARTICLE INFO

Keywords:
Heritage structures
Masonry elements
TRM strengthening
In-plane response
Out-of-plane behaviour

ABSTRACT

This paper presents detailed experimental and analytical investigations into the influence of textile-reinforced mortar (TRM) strengthening on the in-plane and out-of-plane response of unreinforced heritage masonry (URM) elements. The URM wall elements consist of hydraulic lime mortar and fired-clay bricks, and the TRM reinforcement employs mortar-embedded layers of alkali age-resistant glass meshes. Apart from the material characterisation tests on mortars, bricks, and TRM coupons, the experimental programme includes axial compression tests on wallettes, diagonal compression tests on square panels, as well as four-point bending tests on rectangular panels. In the latter, the bending loads are applied either parallel or perpendicular to the bed joints in order to assess the joint layout effect on the behaviour. With the aid of digital image correlation, the in-plane and out-of-plane enhancement in stiffness, strength, and ductility of the masonry elements due to the TRM strengthening is quantified, while the TRM influence on the crack patterns and failure modes is also examined. The results show that the number of mesh layers has a significant influence on the behaviour for the out-of-plane bending tests but plays a less pronounced role in the in-plane shear cases. Modified analytical models for the in-plane shear and out-of-plane bending capacities of reinforced masonry elements, of the type examined in this study, are also proposed and assessed alongside existing codified procedures. The application of current code provisions results in overly conservative estimates. In contrast, the proposed analytical approaches for determining the in-plane and out-of-plane strength provide close prediction of the experimental capacities from this study as well as those from a wider collated database of previous tests, and are therefore suitable for implementation in practical assessment and rehabilitation guidelines.

1. Introduction

Heritage unreinforced masonry (URM) structures are characterised by simplistic structural typologies, irregular bearing elements and high material heterogeneity, as well as time-dependent degradation [1–3]. Their structural performance depends on multiple factors such as the boundary and loading conditions, bond pattern, aspect ratio, and material properties, among others [4,5]. Such buildings are typically able to withstand gravity loads and are susceptible to substantial damage under lateral loading [6]. Irregular component geometry and insufficient connections between horizontal and vertical elements can lead to the formation of out-of-plane instabilities [7,8]. Material heterogeneity, permanent moisture, and environmental degradation also influence the in-plane stiffness, strength, and deformation capacity of the masonry [9, 10]. URM in-plane response is largely characterised by shear sliding, diagonal cracking, or compressive crushing, commonly defining shear-compression limit state domains [11]. Depending on the boundary conditions, out-of-plane URM mechanisms broadly involve either a crack at mid-span or a simply supported cantilever response [12].

To prevent failure, URM walls are typically strengthened by inserting reinforcement within the bed joints or by surface strengthening [13]. The latter includes the adoption of fibre reinforced polymers (FRP) bonded with epoxy to the masonry substrate, or reinforcement meshes embedded in mortars laid on the substrate. In the latter case, the meshes can be made of steel, or natural fibres [14,15]. FRPs have the drawback of limited mechanical compatibility between the masonry and strengthening materials [16,17]. Thus, reinforcing meshes, particularly glass, carbon, and basalt fibre-based, are more suitable for strengthening heritage URM. These are typically referred to as fibre/fabric reinforced

* Corresponding author at: Dept of Civil and Environmental Engineering, Imperial College London, UK.
E-mail address: a.elghazouli@ic.ac.uk (A.Y. Elghazouli).

https://doi.org/10.1016/j.conbuildmat.2024.138152
Received 23 March 2024; Received in revised form 25 July 2024; Accepted 29 August 2024

Notation

Latin uppercase

A_f	shear-effective area of fibres per side of the wall
E_f	elastic modulus of fibres
E_m	elastic modulus of masonry
E_r	elastic modulus of overlay mortar
F	force from the actuator
F_u	ultimate (peak) force from the actuator
G	shear stiffness modulus
K_{x1}	stiffness of masonry tested parallel to the bedding joints
K_{x2}	stiffness of masonry tested perpendicular to the bedding joints
L_1	distance between supports for specimens tested in bending
L_2	distance between load application points for specimens tested in bending
M	moment capacity according to the proposed approach
M_{ACI}	moment capacity according to the American code
M_{CNR}	moment capacity according to the Italian code
M_{EC}	moment capacity according to the European-based approach
$M_{\exp}$	moment capacity from testing
M_m	URM bending resistance
N	axial force in section (positive for tension)
$V_{\exp}$	shear capacity from testing
V_m	URM shear resistance
V_{sc}	masonry crushing shear resistance
$V_{t,ACI}$	TRM contribution to shear capacity according to the American code
$V_{t,CNR}$	TRM contribution to shear capacity according to the Italian code
$V_{t,\exp}$	TRM contribution to shear capacity from testing
V_{tr}	TRM contribution to shear capacity according to the proposed approach

Latin lowercase

b	correction factor for the shear stress distribution in the middle section of the wall
d	effective thickness of the wall in bending
f_b	compressive strength of brick unit
f_{bu1}	compressive strength of brick unit parallel to the testing bed
f_{bu2}	compressive strength of brick unit perpendicular to the testing bed
f_j	compressive strength of joint mortar
f_m	masonry compressive strength
f_r	compressive strength of overlay mortar
f_t	diagonal tensile strength of masonry
$f_{t,r}$	overlay mortar tensile strength
$f_{t,TRM}$	TRM tensile strength
f_x	flexural tensile strength of masonry
h	height of the wall
l	width of the wall
l_x	length of horizontal virtual gauge
l_y	length of vertical virtual gauge
l_f	design dimension of the reinforcement perpendicular to the shear force
n_f	number of fibre layers on one side of the wall
n_s	number of sides of the wall that are strengthened
t	thickness of the wall
t_{eff}	effective thickness of a fibre layer
t_r	thickness of overlay mortar layer per side of the wall
t_{Vf}	equivalent thickness of a fibre layer
x	neutral axis depth according to the proposed approach
x_{ACI}	neutral axis depth according to the American code
x_{CNR}	neutral axis depth according to the Italian code
x_{EC}	neutral axis depth according to the European-based approach
w_a	water absorption rate

Greek letters

α_t	coefficient that considers the reduction in the fibres tensile strength when loaded in shear
β	reduction factor applied to the neutral axis depth for the stress block diagram
β_{sc}	factor accounting for the confinement that the TRM provides to the wall
γ	reduction factor applied to the compressive strength of masonry for the stress block diagram
γ_u	ultimate shear strain
δ	corrected mid-span displacement considering relative displacement at the supports
δ_u	ultimate (peak) displacement
δ_x	displacement recorded from horizontal virtual gauge
δ_y	displacement recorded from vertical virtual gauge
ε_{fd}	design axial fibres strain
ε_{fe}	extreme axial fibres strain
ε_{fu}	ultimate axial fibres strain
$\varepsilon_{\mathrm{lim},conv}$	conventional strain limit for failure due to end debonding
$\varepsilon^{(\alpha)}_{\mathrm{lim},conv}$	conventional strain limit for failure due to intermediate debonding
ε_{md}	design yield strain
ε_{me}	extreme axial strain at masonry
ε_{mu}	ultimate masonry axial strain
ε_{m1}	masonry vertical crushing strain
ε_{m2}	masonry lateral crushing strain
ε_r	strain at overlay mortar
$\varepsilon_{u,TRM}$	ultimate axial strain of TRM
σ_r	stress at overlay mortar
σ_0	precompression stress
τ_u	ultimate shear stress

cementitious mortars (FRCM) or textile-reinforced mortars (TRM). Compared to other traditional strengthening techniques, TRM offers advantages through its high tensile strength-to-weight ratio, providing deformability to masonry by restricting crack widening both for in-plane and out-of-plane actions [18].

In plane, under diagonal tension, the textile contribution is limited at the pre-cracking stages due to strain compatibility in the composite, and the mortar overlay acts as a stiffness enhancer [19,20]. After cracking in the TRM, the deformation is mainly carried by the textile mesh [21,22]. The in-plane response is typically assessed through panel tests in diagonal compression [23]. TRM incorporating high strength meshes provides an increase in both strength and ductility. Previous tests showed that panels strengthened on one or both faces with glass TRM had an average of 131 % and 463 % higher strength than their non-strengthened counterparts [23]. Similar strengthening configurations led to shear strength enhancements above 400 % [24]. The in-plane shear capacity, however, is limited by the diagonal crushing of the masonry [25].

For out-of-plane bending, the thickness of the mortar has limited influence, as the failure is consistently governed by mesh rupture at the tension side of the wall [26]. Weaker meshes provide lower strength increase but higher deformation capacity, whilst stronger meshes provide more strength, but less deformation capacity [27]. Moreover, textile mesh epoxy-resin coating increases the masonry capacity compared with uncoated cases [28]. With respect to performance enhancement, out-of-plane strengths of glass TRM reinforced panels were shown in earlier studies to be 3.7 times greater than those of URM fired clay brick masonry walls [26]. On the other hand, carbon TRM increased the out-of-plane strength and deformability of the URM walls by 10 and 4 times, respectively, compared to a counterpart with only render mortar [17]. The use of GFRP mesh allowed the resistance of out-of-plane bending moments 4–5 times higher than those of URM counterparts, enabling deflections more than 25 times greater by effectively limiting crack openings [29]. Coated basalt TRMs provided strength enhancement of 1.9 and 1.5 times in single- and double-leaf walls, respectively [28]. These previous studies also showed that the strength increases with the number of layers, but there is typically an upper threshold imposed by other limiting failure conditions in masonry.

Whilst research has been carried out on both in-plane and out-of-plane response of TRM-strengthened masonry, most studies have not consistently investigated both actions for the same specimen configuration. There is also a need for more detailed assessment into the influence of TRM strengthening and the effect of multilayer textile arrangements on the masonry response. Importantly, there is a lack of standardised and consistent approaches to quantify the benefits of TRM systems on the performance of masonry, and existing analytical models are unable to estimate the strength properties effectively. Moreover, existing design expressions are validated on a specific test series or datasets of a limited range of parameters, which may not be suitable for heritage structures.

This paper presents an experimental and analytical study into the in-plane and out-of-plane response of URM with material properties characteristic of existing structures in Historic Cairo and other thirteen century masonry buildings [9,30,31]. The investigation focuses on the influence of TRM-strengthening on the behaviour. After describing the experimental procedures, the results from material and wall element tests are presented. These include tests on bricks, mortars, and TRM coupons, as well as compression wallettes, panels in diagonal compression, and walls in bending perpendicular and parallel to the bed joint direction. The test results from this paper, combined with those from a collated database, are used for validation of design expressions under in-plane and out-of-plane actions. A modified approach which adopts consistent ultimate strain limits for the shear and bending design of TRM-strengthened masonry is proposed, as current guidance is shown to result, on average, in either overly conservative or unsafe results.

2. Experimental methods

2.1. Constituent materials

A hydraulic binder (NHL5), containing calcium hydroxide, calcium aluminates, and silicates, was employed in the lime mortars. NHL5 is produced by firing crushed marl limestone in kilns [32]. Following this process, the limestone undergoes slaking also referred to as hydration. This process involves controlled addition of water and subsequent grinding into powders [33]. These binders possess unique characteristics, combining hydraulic properties with air settings that are achieved through carbonation with atmospheric CO_2 [34]. The NHL5 binder has a specific gravity of 2.70, and a content of free lime exceeding 15 %, while the content of sulphates remains below 2 % [32,35]. Soft sand was used as aggregate for the composition of bed joint and overlay mortars. In contrast to sharp sand, this type of sand has rounded particles of size below 1.0 mm, ensuring improved mix workability [36]. The specific gravity of the sand was 2.65, and its moisture content around 5 %.

With the aim of replicating the properties of heritage buildings in Old Cairo, NHL5 was combined with bricklaying sand at a 1:3.25 ratio for bed joint mortars. The overlay mortars had equal quantities of cement and lime, and a binder-to-aggregate ratio of 1:4.5, while no additives were included. The cement ensures high strength and stiffness, providing mechanical compatibility with the masonry substrate, whilst the lime ensures deformability. In all mortars, the water-to-binder ratio was around 1.0. The water quantity was adjusted to ensure workability, with a targeted flow diameter of 180–190 mm. The mortars were prepared in batches of 20 litres with a 40 litres rotary mixer, in the following order: 180 s mixing of the dry constituents, addition of water and mixing for another 180 s, and removal from the mixer and either used in bed joints or overlays, or as samples for assessment of material properties. All samples were kept in laboratory conditions and covered in plastic sheets to ensure adequate curing conditions. Around 120 × 50 mm cube tests were carried out to evaluate the compressive strength of the mortars used in the bed joints and overlays, with a minimum of three samples per masonry specimen.

Solid bricks of 229 × 108 × 66 mm and a specific weight of 17.1 kN/m^3 were used for the construction of all walls. These were fired-clay bricks with physical and mechanical properties closely resembling those of the bricks found in the Mausoleum of Fatima Khatun (Umm al-Salih) in Cairo [30,31,36]. They had a nominal compressive strength (f_b) of 21 MPa when tested parallel to the bed face as described in Section 3, and a water absorption rate (w_a) of 10 % [37,38]. Prior to testing, to ensure planeness and parallelism, the faces in contact with the support/loading plates or bearings were ground.

For strengthening purposes, an alkali and age-resistant coated glass fibre reinforcing mesh (CT325) was used [39]. The mesh had a 4.0 × 4.0 mm grid, a cross-sectional area of 31 mm^2/m, and a nominal tensile strength of 2075 N/5 cm in the warp direction, and 2180 N/5 cm in the weft direction. Although the grid spacing was dense compared to typical commercial spacings reported in ACI 549.6 [40], it was selected based on similar grid spacings in previous studies [41,42] and it was ensured that adequate adhesion between the grid layers and the substrate was achieved during construction of the specimens, using high-density polyethylene anchors. The mesh (glass fibres with coating) had a weight of 160 g/m2 and elongation at failure of 3 %. The elastic modulus of the glass fibres was 72 GPa and their density was 2.58 g/cm^3.

A total of 6 × 50 mm wide and 450 mm long prismatic TRM samples (3 samples with one layer and 3 samples with two layers of textile mesh in lime-cement mortar) were prepared and tested in direct tension following EN 13934–1:2013 [43], to assess the full deformational response of the TRM overlay. The mesh was embedded at the two ends into 75×50×10 mm (length × width × thickness) lime-cement mortar tabs. The non-embedded mesh region had a length of 300 mm. The samples were fabricated in plastic moulds by adding the mortar and textile meshes gradually, following guidance available in the literature [44,45]. Additionally, 6 bond tests between TRM overlay and masonry substrate, with 3 samples incorporating one layer and another 3 incorporating two textile layers, were carried out on single-brick single-lap systems to assess the likelihood of substrate-to-TRM debonding. This configuration was considered as opposed to masonry prisms, as single-brick single-lap tests provide a lower bound of the bond strength, considering that bed joints have a positive effect on the TRM in-plane bond strength [46,47]. As in the tension TRM coupons, the width of the mortar component was 50 mm, and was bonded to the substrate over a length of 200 mm. Prior to placing the first layer of mortar, the surface was brushed, cleaned with compressed air, and painted with a thin film of cement slurry. All TRM samples were covered in plastic sheets to maintain a controlled environment and ensure the same conditioning as in the case of mortar cubes. Apart from direct tension and bond tests on TRM coupons, 3 mesh-only tension tests were also performed, with a single layer of mesh. Further information on these tests can be found in previous work by the authors [48].

2.2. Masonry specimens

Four types of masonry panels, as shown in Fig. 1, were investigated in this study: namely, wallettes tested in axial compression, square panels tested in diagonal compression, and rectangular panels tested in four-point bending with the loading applied parallel or perpendicular to the bed joints. The last two types of tests are referred to as 'bending parallel' and 'bending perpendicular', respectively, in this paper. All tests were performed in displacement control for obtaining a detailed insight into the crack initiation and propagation, as well as the overall failure kinematics.

Axial compression tests on twelve URM wallettes of average measured dimensions $l \times h \times t = 460 \times 377 \times 108$ mm were carried out to assess the compressive strength of masonry (where l is the width, h is the height, and t is the thickness), following the guidelines in EN 1052–1:1999 [49]. These were separated into groups of four specimens, with each group tested at the same time while each of the groups of square panels in diagonal compression, the bending parallel, and the bending perpendicular tests were conducted. More specifically, the test of Wallettes WDa-WDd (Group WD) were carried out simultaneously with the diagonal compression tests, Wallettes WBPRa-WBPRd (Group WBPR) were tested at the same time as the bending parallel walls, and Wallettes WBPPa-WBPPd (Group WBPP) were tested along with the bending perpendicular walls. Details of these specimens are given in Table 1.

A total of nine square panels of $l \times h \times t = 688 \times 688 \times 108$ mm were tested in diagonal compression, based on the recommendations in ASTM E519–07 [50]. These tests aimed to investigate the influence of mesh thickness on strength, validate expressions for diagonal tension strength, and assess the practicality of multi-layer mesh overlays. They comprise three URM panels (Group D0, with Wall Specimens D0a, D0b, and D0c), three panels with one mesh layer at each side (Group D1, with Wall Specimens D1a, D1b, and D1c), and three panels with two layers of mesh at each side (Group D2, with Wall Specimens D2a, D2b, and D2c). The TRM thickness for each side was on average 13 mm and 15 mm for one and two mesh layers, respectively. Details of the walls in each group are given in Table 2.

Nine walls of average measured dimensions $l \times h \times t = 460 \times 917 \times 108$ mm were tested in bending with the mortar joints running parallel to the direction of loading, along the width of the specimen. Three of these were URM (Group BPR0, with Wall Specimens BPR0a, BPR0b, and BPR0c), two had one mesh layer at each side (Group BPR1, with Wall Specimens BPR1a, and BPR1b), and four had two mesh layers at each side (Group BPR2, with Wall Specimens BPR2a, BPR2b, BPR2c, and BPR2d). The measured TRM thickness for each side was on average 12 and 15 mm for one and two mesh layers, respectively. Details of the specimens are provided in Table 3.

To investigate the effect of the brick arrangement on the bending performance of masonry walls, a series of nine wall specimens of average measured dimensions $l \times h \times t = 450 \times 932 \times 108$ mm were subjected to four-point bending tests with the mortar joints being perpendicular to the loading direction, running along the height of the specimens. Three groups of walls were defined: URM without mesh (Group BPP0, with Wall Specimens BPP0a, BPP0b, and BPP0c), with one mesh layer at each side (Group BPP1, with Wall Specimens BPP1a, BPP1b, and BPP1c), and with two layers of mesh at each side (Group BPP2, with Wall Specimens BPP2a, BPP2b, and BPP2c). The measured TRM thickness for each side was on average 15 and 16 mm for one and two mesh layers, respectively. Details of the walls in each group are given in Table 4. The bending tests with both brick arrangements were carried out based on EN 1052–2:2016 [51].

All masonry elements were constructed with lime mortar bed joints measuring approximately 10 mm in thickness. Before testing, the specimens were hydrated by sprinkling water and then covered in plastic sheets until testing. For the strengthened specimens, the procedure included applying a primer film, drilling anchor holes without inserting epoxy resin, applying a base overlay, inserting the textile mesh, inserting anchors, and then applying the final coat. For the multi-layer specimens, a thin layer of mortar, approximately 4±1.0 mm thick, was added between each textile layer. To improve the shear connection and prevent debonding between the textile and the substrate, eight, eleven, and twelve anchors were symmetrically positioned, as shown in Fig. 1. The anchors had 8 mm diameter and 52 mm length, and featured a disc with a 60 mm diameter at the top. The thickness of the overlay varied depending on the number of mesh layers as described above. The curing period of masonry members was approximately 60 days, which allowed the bed joint mortar to develop sufficient strength. The rendering of the strengthened specimens was completed 14 days before the start of testing, which lasted approximately one month. Hence, the age of the TRM overlays varied between 14 and 40 days. Tests on mortar overlay and bed joint samples were carried out on the day of testing of the corresponding wall elements.

2.3. Testing arrangements and instrumentation

During each test, the response of the specimens was measured using transducers. Additionally, displacement recordings were obtained from the loading actuators, and data from the digital image correlation (DIC) system was also collected. The DIC system, which offers a high level of accuracy and practicality compared to traditional mechanical instruments [52,53], consisted of two lightweight CMOS cameras with a resolution of 2.3 Megapixels. They were connected to a controller that served as a data acquisition system. As part of the preparation process, the specimens were painted in white and then speckled with 0.5–2.0 mm black dots.

Before conducting the tests, a calibration procedure was performed.

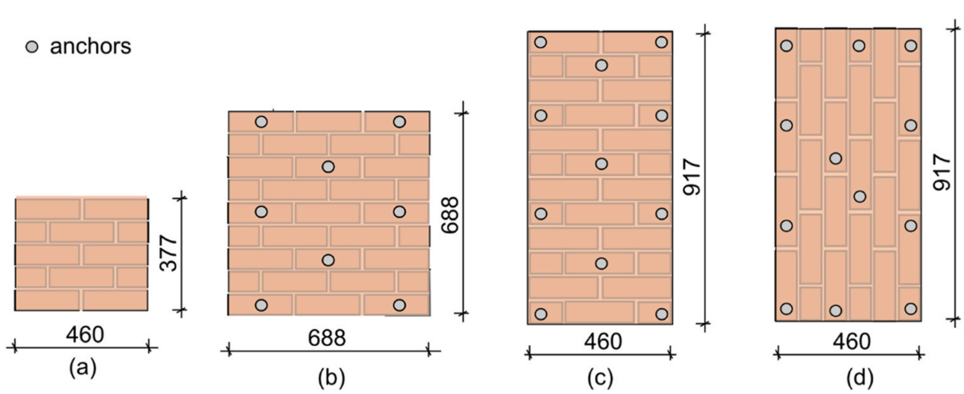

Fig. 1. Schematic representation of: (a) wallettes for axial compression tests, (b) square panels for diagonal compression tests, (c) rectangular panels for bending parallel tests, and (d) rectangular panels for bending perpendicular tests.

Table 1
Main test results from compression tests on URM wallettes (W specimens).

ID	F_u (kN)	δ_u (mm)	f_m (MPa)	ε_{m1} (%)	ε_{m2} (%)	E_m (MPa)	f_j (MPa)
WDa	323.91	4.50	6.53	0.47	0.29	1650.32	1.76±0.27
WDb	319.99	3.97	6.46	0.64	0.37	1468.82	1.77±0.21
WDc	322.07	4.83	6.50	0.51	0.81	1584.55	1.77±0.16
WDd	293.37	5.10	5.92	0.40	0.22	1389.27	1.73±0.15
WD (avg)	314.83	4.60	6.35	0.51	0.42	1523.24	1.76
WD (stdev)	±14.40	±0.49	±0.29	±0.10	±0.27	±116.64	±0.2
WD (COV)	4.57	10.65	4.57	19.61	64.29	7.66	11.36
WBPRa	360.81	4.91	7.28	0.80	0.33	1294.78	1.11±0.26
WBPRb	345.39	4.86	6.84	0.63	0.52	1452.52	1.11±0.26
WBPRc	320.25	4.47	6.46	0.61	0.39	1909.66	1.37±0.37
WBPRd	340.83	4.43	6.78	0.66	0.48	1266.04	1.63±0.27
WBPR (avg)	341.82	4.67	6.84	0.68	0.43	1480.75	1.3
WBPR (stdev)	±16.73	±0.25	±0.34	±0.09	±0.08	±297.46	±0.29
WBPR (COV)	4.89	5.35	4.97	13.24	18.60	20.09	22.31
WBPPa	366.92	5.10	7.40	0.51	0.08	2066.78	1.85±0.32
WBPPb	334.05	4.29	6.71	0.69	0.45	1327.06	2.08±0.19
WBPPc	339.78	4.32	6.88	0.47	0.50	1920.54	2.08±0.19
WBPPd	347.47	4.31	6.96	0.62	0.28	1234.79	1.76±0.27
WBPP (avg)	347.05	4.50	6.99	0.57	0.33	1637.29	1.94
WBPP (stdev)	±14.34	±0.39	±0.29	±0.10	±0.19	±417.51	±0.24
WBPP (COV)	4.13	8.67	4.15	17.54	57.58	25.50	12.37

Table 2
Main test results of URM and TRM-strengthened panels in diagonal compression (D specimens).

ID	n_f (-)	F_u (kN)	δ_u (mm)	τ_u (MPa)	γ_u (%)	G (MPa)	f_j (MPa)	f_r (MPa)
D0a	0	52.77	2.15	0.51	0.11	515.72	0.97±0.13	-
D0b	0	48.06	2.59	0.46	0.12	527.63	1.08±0.13	-
D0c	0	36.77	2.11	0.36	0.11	390.72	1.28±0.17	-
D0 (avg)		45.87	2.29	0.44	0.11	478.02	1.11	-
D0 (stdev)		±8.22	±0.27	±0.08	±0.00	±75.84	±0.15	-
D0 (COV)		17.92	11.79	18.18	0.00	15.87	13.51	-
D1a	1	170.35	5.36	1.33	0.10	2105.86	1.14±0.15	8.29±0.38
D1b	1	178.84	5.44	1.37	0.08	2673.58	1.37±0.22	7.00±0.89
D1c	1	173.38	5.11	1.38	0.06	3654.00	1.47±0.16	8.74±0.81
D1 (avg)		174.19	5.30	1.36	0.08	2811.15	1.33	8.01
D1 (stdev)		±4.30	±0.17	±0.02	±0.02	±783.18	±0.18	±0.69
D1 (COV)		2.47	3.21	1.47	25.00	27.86	13.53	8.61
D2a	2	203.31	5.57	1.51	0.11	2500.20	1.45±0.21	11.79±0.89
D2b	2	194.97	5.35	1.50	0.05	3295.31	1.49±0.23	8.75±1.07
D2c	2	190.56	5.60	1.40	0.06	3069.48	1.21±0.36	9.63±1.29
D2 (avg)		196.28	5.51	1.47	0.07	2955.00	1.38	10.06
D2 (stdev)		±6.48	±0.14	±0.06	±0.03	±409.73	±0.27	±1.08
D2 (COV)		3.30	2.54	4.08	42.86	13.87	19.57	10.74

This involved adjusting the aperture, ambient lighting, and camera focus through iterative adjustments while capturing photos of a calibration plate placed next to the surface of the specimen. A data recording frequency of 0.5 Hz was selected during the tests to ensure a sufficiently large dataset and minimize potential variations. Subsequently, the DIC data obtained from the tests were subjected to further processing in order to obtain deformation vector fields. From these fields, surface strains or deformations were evaluated using virtual gauges with different lengths, as detailed below.

The cubic mortar samples were tested in an Instron machine with a capacity of 100 kN at a displacement rate of 1 mm/min, whilst the bricks were tested in a Control Automax machine at a loading rate of 0.6 MPa/s. The mesh and TRM coupon tensile tests were carried out in an Instron 250 kN machine under displacement control at a rate of 0.25 mm/min in the elastic regime and at a rate of 1.0 mm/min in the cracked stage. The single-lap bond tests were carried out in the same machine at a displacement rate of 0.1 mm/min, and the brick was tied to the machine bed by means of steel plates and threaded rods, to ensure alignment of the mesh central to the axis of the machine. To facilitate gripping during testing, in the direct tension and bond tests, the ends of the TRM samples were provided with 1 mm thick aluminium tabs glued with a 2-part epoxy resin. The mesh and TRM tensile tests and the single-lap bond tests were conducted using a purpose-made rig depicted in Fig. 2, which was design based on available guidance [44,54]. The DIC system was used to record the sample behaviour and the machine was used to record the force corresponding to the applied displacement.

The wallettes were tested in axial compression in an Instron 3500 kN machine at a rate of 0.5 mm/min, as shown in Fig. 3a. The arrangement included a steel transfer plate between the actuator and the specimen. A thin timber panel was used to ensure uniform contact between the base of the machine and the wallette. Two displacement transducers were positioned around the specimen to record its axial shortening. Two vertical virtual gauges of 150 mm, and one horizontal virtual gauge of 240 mm length were also defined during postprocessing of the DIC data, as illustrated in Fig. 3b. These were used to obtain axial and horizontal strains, respectively.

The diagonal compression tests were conducted at a rate of 0.5 mm/min using a modular steel frame which was provided with a 1000 kN Instron actuator and associated load cell, as shown in Fig. 4a. To transfer the load from the actuator, steel V-shaped supports were positioned at the top and bottom of the square panel. Thin timber panels were added between the steel supports and masonry specimen to ensure uniform contact. At the top, a hinge was provided to avoid any out-of-plane loading. Two external transducers were used to measure the axial and

Table 3
Main test results of URM and TRM-strengthened wall elements tested in bending acting parallel to the bed joint (BPR specimens).

ID	n_f (-)	F_u (kN)	δ_u (mm)	K_{x1} (kN/mm)	f_j (MPa)	f_r (MPa)
BPR0a	0	1.04	0.17	12.82	1.81 ±0.18	-
BPR0b	0	1.77	0.20	7.39	2.04 ±0.26	-
BPR0c	0	0.92	0.14	11.88	1.63 ±0.42	-
BPR0 (avg)		1.24	0.17	10.70	1.72	-
BPR0 (stdev)		±0.46	±0.03	±2.90	±0.3	-
BPR0 (COV)		37.10	17.65	27.13	17.44	-
BPR1a	1	11.63	1.74	24.88	2.09 ±0.39	10.00 ±2.16
BPR1b	1	11.95	3.45	34.85	1.96 ±0.33	12.16 ±2.14
BPR1 (avg)		11.79	2.60	29.87	2.03	11.08
BPR1 (stdev)		±0.23	±1.21	±7.05	±0.36	±2.15
BPR1 (COV)		1.95	46.54	23.61	17.73	19.40
BPR2a	2	22.16	6.96	61.47	2.09 ±0.34	9.25 ±0.63
BPR2b	2	24.73	4.81	60.61	2.34 ±0.42	5.96 ±0.63
BPR2c	2	22.84	4.84	44.06	1.92 ±0.54	6.73 ±0.66
BPR2d	2	20.41	3.79	76.53	1.68 ±0.17	8.84 ±0.89
BPR2 (avg)		22.54	5.10	60.67	2.01	7.69
BPR2 (stdev)		±1.78	±1.33	±13.27	±0.37	±0.70
BPR2 (COV)		7.90	26.08	21.87	18.41	9.10

Table 4
Main test results of URM and TRM-strengthened wall elements tested in bending acting perpendicular to the bed joints (BPP specimens).

ID	n_f (-)	F_u (kN)	δ_u (mm)	K_{x2} (kN/mm)	f_j (MPa)	f_r (MPa)
BPP0a	0	3.43	0.41	16.00	1.27 ±0.14	-
BPP0b	0	3.81	0.66	11.38	1.63 ±0.40	-
BPP0c	0	3.73	0.66	12.98	2.00 ±0.16	-
BPP0 (avg)		3.65	0.57	13.45	1.63	-
BPP0 (stdev)		±0.20	±0.15	±2.35	±0.23	-
BPP0 (COV)		5.48	26.32	17.44	14.11	-
BPP1a	1	12.87	1.14	43.69	1.81 ±0.17	10.58 ±2.65
BPP1b	1	12.46	0.58	50.71	1.65 ±0.23	9.65 ±1.92
BPP1c	1	13.81	1.46	47.23	2.21 ±0.26	11.87 ±1.59
BPP1 (avg)		13.05	1.06	47.21	1.89	10.7
BPP1 (stdev)		±0.69	±0.45	±3.51	±0.22	±2.05
BPP1 (COV)		5.29	42.45	7.43	11.64	19.16
BPP2a	2	21.99	3.50	86.17	1.57 ±0.15	11.83 ±1.15
BPP2b	2	21.70	3.50	50.61	1.86 ±0.06	10.43 ±2.11
BPP2c	2	22.23	2.81	40.56	2.55 ±0.31	5.85 ±1.04
BPP2 (avg)		21.98	3.27	59.11	1.99	9.37
BPP2 (stdev)		±0.26	±0.40	±23.96	±0.17	±1.43
BPP2 (COV)		1.18	12.23	40.54	8.54	15.26

transverse strain, whilst two virtual gauges of length 885 mm were also defined, as shown in Fig. 4b.

Four-point bending tests were performed in a testing arrangement that included a loading transfer frame with a 1000 kN Instron actuator and load cell, under displacement control at a rate of 0.5 mm/min. The rigs are shown in Figs. 5a and 6a, for the parallel and perpendicular cases, respectively. The specimens were placed on a timber panel and pin-supported at the top and bottom. The load was applied from the actuator by means of two hinges, which were located at a distance equal to one-third of the specimen height from its ends. This symmetrical configuration resulted in a constant bending moment between the load application points. Six external transducers were used to measure the displacements at the supports and load application points, as shown in Figs. 5b and 6b for the bending parallel and bending perpendicular tests, respectively. During the postprocessing of the data from DIC, four virtual gauges of 50 mm length were defined along the critical crack.

3. Test results

3.1. Uniaxial response

The average strengths for the joint mortars varied within f_j=1.27–1.91 MPa as follows: wallettes f_j=1.67±0.24 MPa, BPR specimens f_j=1.91±0.34 MPa, BPP specimens f_j=1.84±0.21 MPa, and D specimens f_j=1.27±0.20 MPa. The average strengths for the overlay mortars were within f_r=9.03–10.03 MPa, as follows: BRP specimens f_r=9.24±1.21 MPa, BPP specimens f_r=10.03±1.74 MPa, and D specimens f_r=9.03±0.89 MPa. The mortar strengths specific for each specimen are listed in Tables 1–4. The lower-strength mortars from the bed joints had a relatively more ductile response with a gradual softening. Overlay mortars had comparatively higher strengths by a factor of around 6, on average, but more brittle response.

The tests on brick units parallel to the testing bed showed an average compressive strength of f_{bu1}=21.30 MPa and a standard deviation of 2.27 MPa. These values were reduced to f_{bu2}=11.52 MPa average strength and 0.49 MPa standard deviation for bricks tested perpendicular to the testing bed. The higher levels of strength obtained in the former case are due to confinement effects related to the low aspect ratio of the specimens, as opposed to those tested perpendicular to the bed face [55]. Note that both f_{bu1} and f_{bu2} are nominal compressive strength, obtained from bricks of average dimensions of 229 × 108 × 66 mm, which were tested according to EN 772–1:2011 [56].

Close inspection of the deformational response showed that TRM coupons were characterised by a trilinear response with an initial elastic response to mortar cracking, and a post-cracking response, as depicted in Fig. 7a. In the figure, the stresses are evaluated using the mesh cross-sectional area. For textile with one layer, this was 1.4 mm^2. The TRM tensile strengths, calculated with respect to the area of the TRM mortar, were $f_{t,TRM}$=2.07±0.03 MPa and $f_{t,TRM}$ =3.78±0.02 MPa for samples with one and two layers, respectively [48]. The respective strengths based on the cross-sectional area of the mesh were 1851±31 MPa and 1800±88 MPa. The deformations at failure were $\varepsilon_{u,TRM}$ =1.31±0.07 % and $\varepsilon_{u,TRM}$ =1.81±0.14 %, for one- and two-layer TRM coupons, respectively, and they were obtained for a gauge length of 400 mm. The cracked elastic modulus was 60953 MPa for samples with one layer and 61223 MPa for samples with two layers. Typical failure modes of the TRM coupons tested in direct tension are shown in Fig. 7b.

The mesh stress-deformation response from bond tests is shown in Fig. 8a, while a representative failure mode is shown in Fig. 8b. Most deformation was concentrated in the mesh with minimal or no

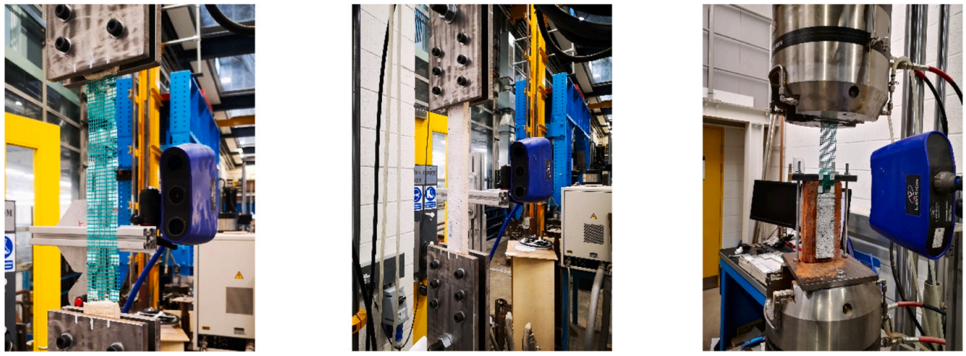

(a) (b) (c)

Fig. 2. Testing arrangement for: (a) mesh tensile coupon samples, (b) TRM tensile coupon samples, and (c) single lap bond tests.

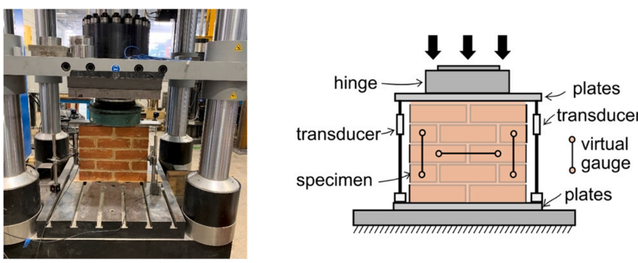

(a) (b)

Fig. 3. Wallette tests: (a) testing arrangement, and (b) schematic representation.

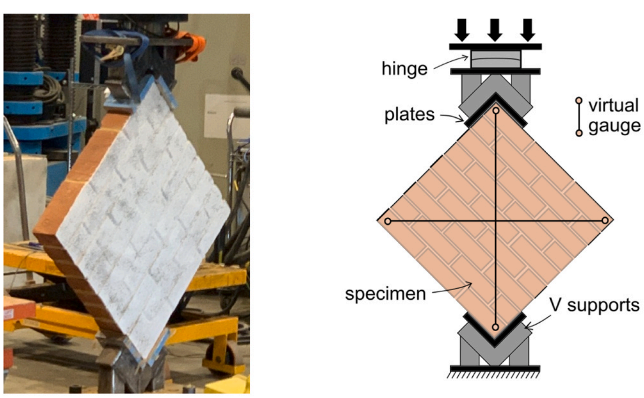

(a) (b)

Fig. 4. Diagonal compression tests: (a) testing arrangement, and (b) schematic representation.

deformations in the TRM, and no slip at the TRM-substrate interface. The average stresses in the textile at rupture were 1193±326 MPa for one layer and 1063±443 MPa for two layers, in both cases lower than the mesh itself that exhibited an average stress of 1360±224 MPa [48]. The corresponding deformations at rupture were 2.39±0.24 % (one layer) and 3.35±0.31 % (two layers), higher than the mesh itself, which showed an average deformation at rupture of 2.19±0.30 % [48]. The compressive strength of the mortar (f_r) from the TRM coupons and bond samples was 13.3±0.71 MPa [48].

The constitutive response of the masonry wallettes obtained from the DIC processing is shown in Fig. 9. Note that the response during testing was also recorded with transducers, which have been used to verify the measurements from the DIC at specific points. The vertical strain, computed as the average strain from the two vertical strain gauges, is plotted on the positive axis, while the lateral strain is shown on the negative axis. The black lines correspond to the average response from the specimens in each figure panel. The post-peak response is plotted until a stress drop of 20 % of the compressive strength. The masonry compressive strength (f_m), the vertical (ε_{m1}) and lateral (ε_{m2}) strain at crushing, and the elastic modulus (E_m), determined at a range of 0–1/3 of the strength, are given in Table 1, along with their average, standard deviation, and coefficient of variation (COV) for each group of specimens. The ultimate (peak) load F_u and the ultimate displacement δ_u recorded during testing are also reported in Table 1. Evidently, the strength of wallettes tested at the same time with the bending tests is very similar (Groups WBPR and WBPP), while the strength is slightly lower for the specimens tested during the diagonal compression tests (Group WD). The mean vertical strain at crushing exceeds the corresponding lateral strain for all groups of wallettes. Finally, the mean elastic modulus is similar in all groups of wallettes and ranges from 1481 to 1637 MPa.

Fig. 10 shows the crack pattern and strain map at failure, obtained from DIC, for Wallette WBPRa. Note that the crack pattern and strain map do not correspond to the maximum load during testing, which is attained before failure. As shown in Fig. 10, two main vertical cracks are discerned at failure, running from the top to the bottom of the wall, near the ends of the actuator. In Wallette WBPRa, the cracking was initiated at mortar joints at the right-hand side and was gradually expanded along the height of the specimen. The formation of the left-hand side crack followed, while more cracks also developed with further application of the load. Asymmetrical cracks were also observed in the rest of the wallettes due to the inherent non-uniformity of the masonry.

3.2. In-plane response

The shear stress-shear strain curves of each group of diagonal compression specimens are plotted in Fig. 11. Grey curves depict results from each wall, while the mean response is shown in black colour. The shear strength (τ_u), ultimate shear strain (γ_u), and shear stiffness modulus (G), determined at a range of 0–1/3 of the shear strength, are given in Table 2, for each specimen, along with the summarised statistics for each group of square panels. The shear stress (τ) and shear strain (γ) were evaluated using Eqs. 1 and 2, respectively. For the calculation of the shear strain, virtual gauges as described in Section 2.3, were used.

$$\tau = \frac{\sqrt{2}F}{2lt} \tag{1}$$

$$\gamma = \left|\frac{\delta_x}{\sqrt{2}\,l_x}\right| + \left|\frac{\delta_y}{\sqrt{2}\,l_y}\right| \tag{2}$$

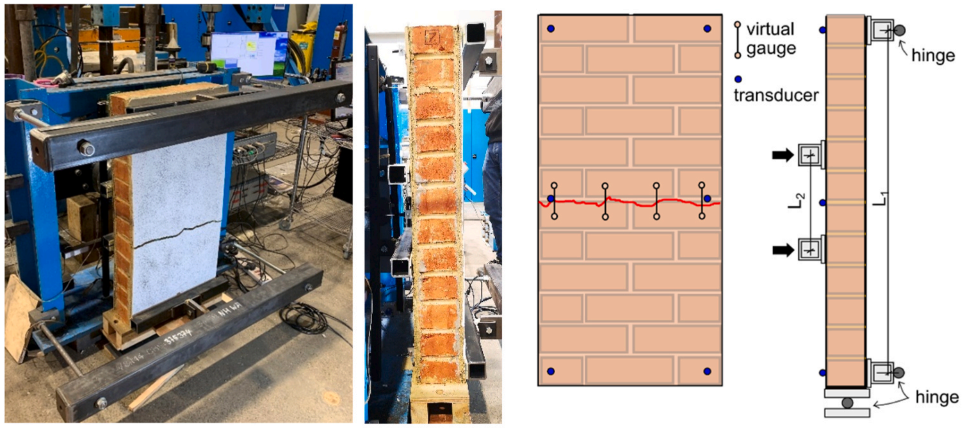

(a) (b)

Fig. 5. Bending parallel tests: (a) testing arrangement, and (b) schematic representation.

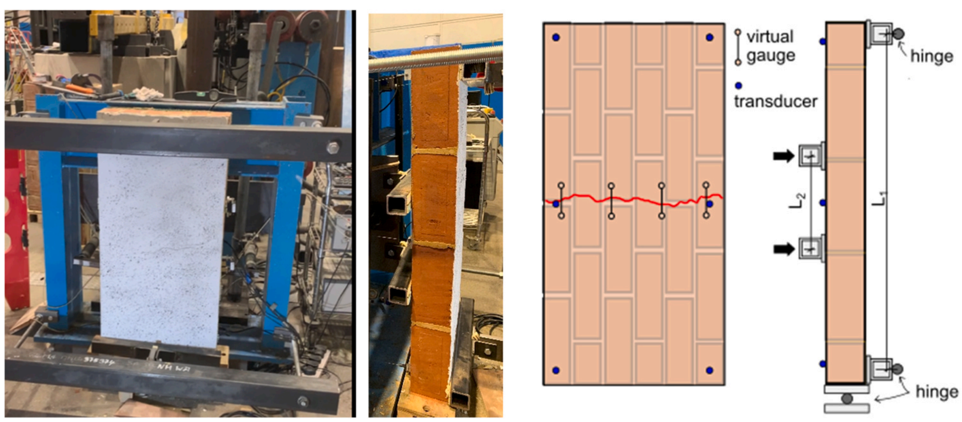

(a) (b)

Fig. 6. Bending perpendicular tests: (a) testing arrangement, and (b) schematic representation.

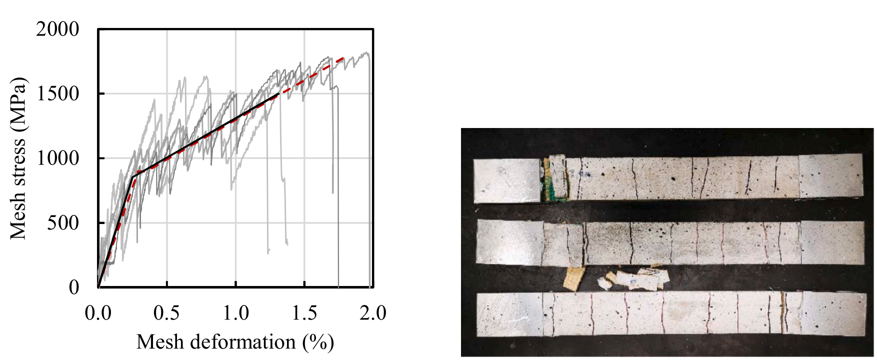

(a) (b)

Fig. 7. Direct tension TRM coupon tests: (a) mesh stress-deformation curves, and (b) typical failure modes.

where F is the force recorded by the actuator, δ_x is the displacement recorded by the horizontal virtual gauge, δ_y is the displacement recorded by the vertical virtual gauge, l_x is the length of the horizontal virtual gauge, l_y is the length of the vertical virtual gauge, l and t are the specimen width and thickness (including the thickness of TRM for strengthened walls), respectively.

The ultimate (peak) load F_u and the ultimate displacement δ_u are also reported in Table 2. The latter represents the vertical displacement corresponding to the peak load and is effectively the same as the displacement δ_y when the peak load F_u is attained.

The shear strength is shown to be significantly higher in TRM-strengthened panels, compared to their URM counterparts, while the specific number of layers of reinforcement appears to be a secondary

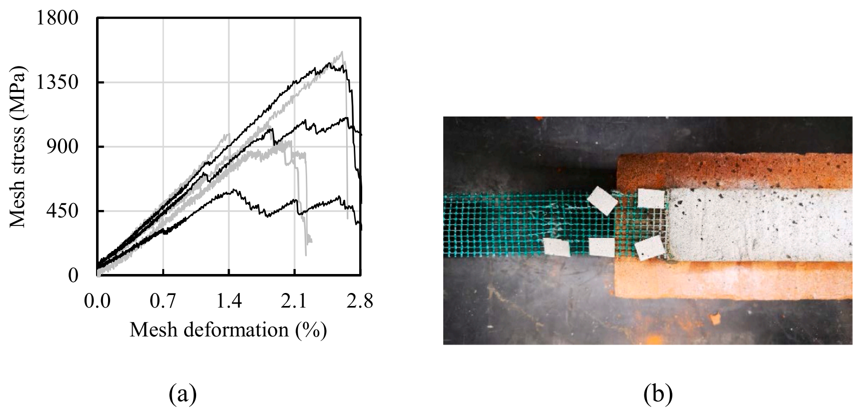

Fig. 8. Bond tests: (a) mesh stress-deformation curves, and (b) typical failure modes.

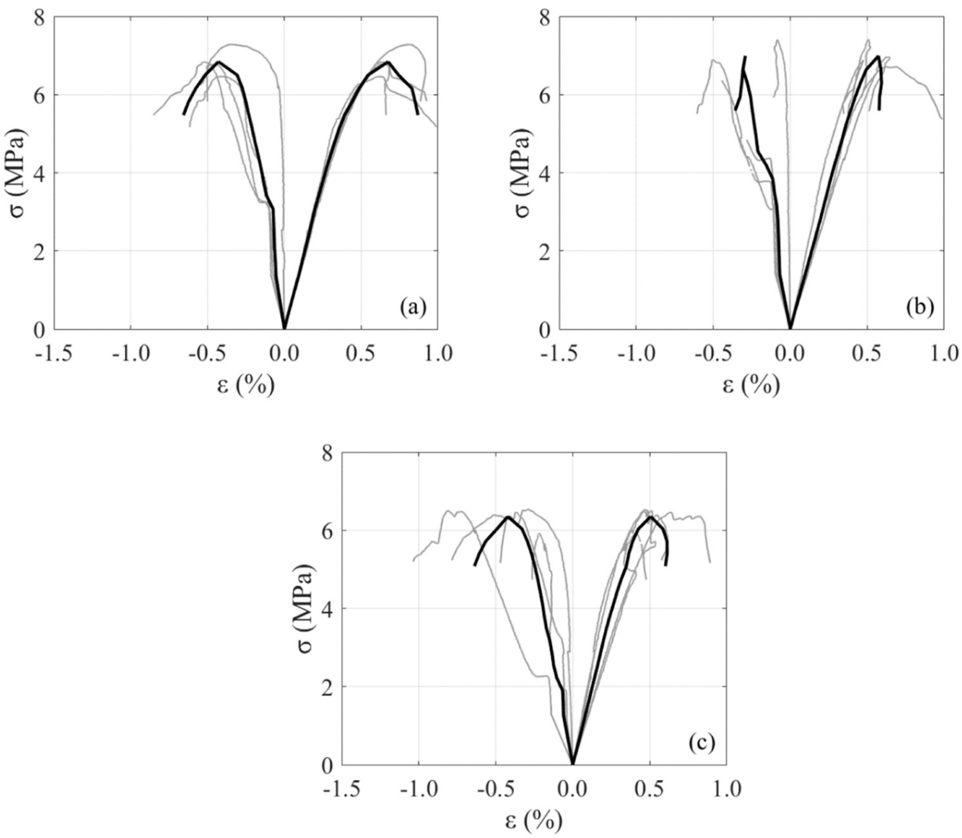

Fig. 9. Axial and lateral stress-strain curves of wallettes: (a) Group WBPR, (b) Group WBPP, and (c) Group WD. Black lines refer to the mean curves and grey lines indicate individual specimens.

parameter, as the ultimate capacity is only slightly reduced when one mesh layer is employed instead of two. More specifically, the shear strength of TRM-strengthened panels is about 3 times higher than the corresponding value attained for the URM panels. Using more layers of textile mesh results in a more ductile response due to the formation of multiple cracks before failure, as discussed below, thus resulting in higher levels of shear strength. The shear stiffness modulus is also considerably higher in TRM-strengthened panels, with average values of about 2900 MPa, compared to their URM counterparts, where it decreases to approximately 500 MPa. Hence, an approximately fivefold increase in the shear modulus may be achieved by textile mesh in masonry wall panels.

Figs. 12 and 13 show typical failure patterns for Specimens D2c and D0a, which are representative of walls with two mesh layers and without mesh, respectively. It should be noted that the crack pattern and strain map depicted in Figs. 8 and 9 correspond to the failure point, towards the end of the test, and not to the peak load reached during testing. In walls with two mesh layers, a more ductile failure was attained, with multiple cracks being formed, until one of these opened, penetrating the masonry substrate and leading to panel failure. As shown in Fig. 12, the critical crack in Specimen D2c ran from the edge of the bottom loading support to a point close to the top support of the specimen. A ductile failure mode was also achieved at walls with one layer of reinforcement, although not shown herein. On the other hand, in the case of URM panels, the failure was due to a main critical stepped crack joining the edges of the top and bottom supports (Fig. 13). Hence, when no mesh was provided, the failure occurred early in a brittle manner, thus justifying the lower ultimate shear strength and shear strain attained in URM

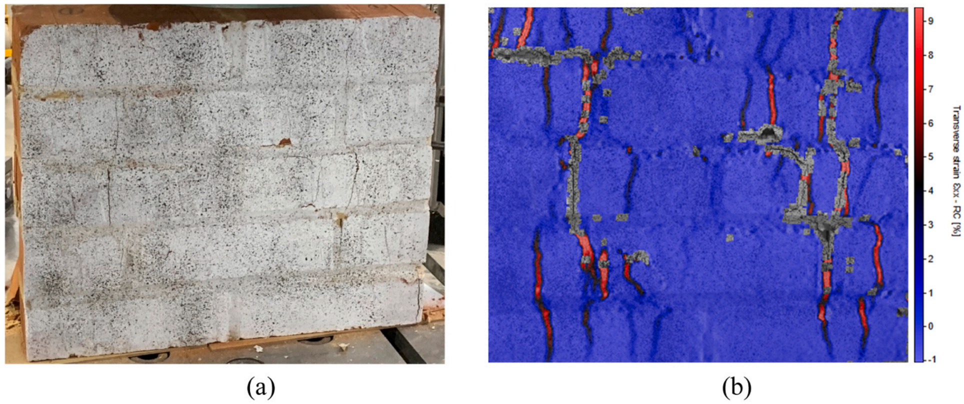

Fig. 10. Failure of Wallette WBPRa (Group WBPR): (a) crack pattern, and (b) strain map from DIC. Red colour indicates cracking or high strain concentration, whilst blue colour indicates low strain levels.

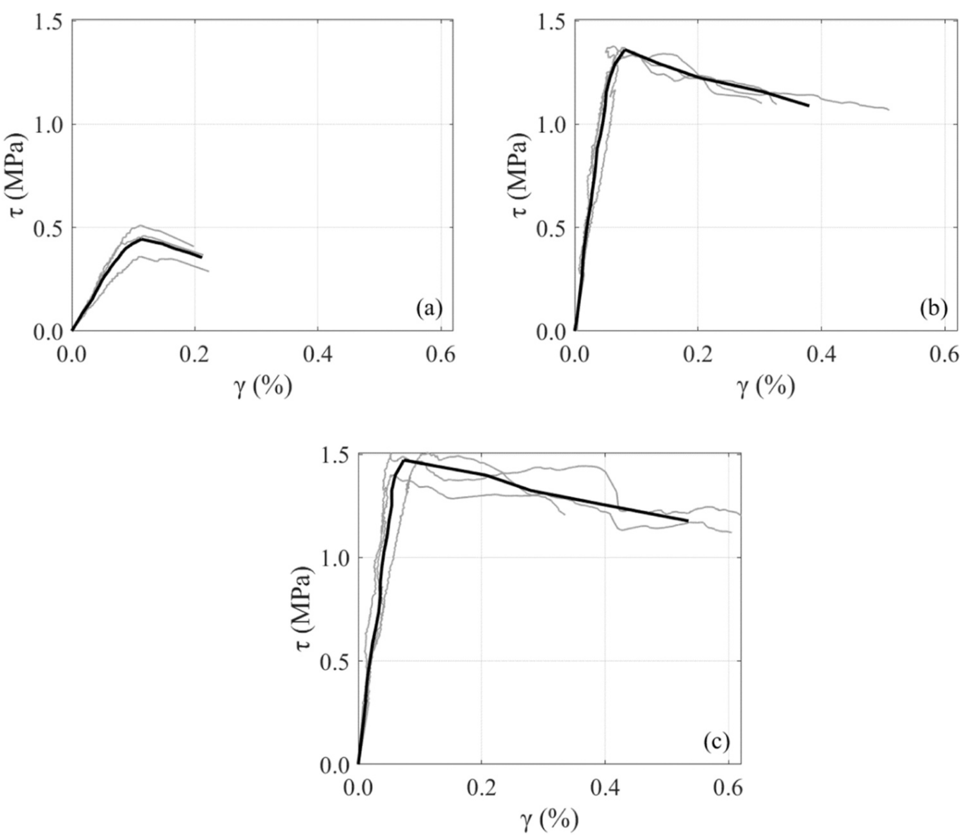

Fig. 11. Shear stress- shear strain curves of diagonals: (a) Group D0, (b) Group D1, and (c) Group D2. Black lines refer to the mean curves and grey lines indicate individual specimens.

panels. This highlights the effectiveness of TRMs in improving the response of masonry walls in diagonal compression, by contributing to an enhanced deformation capacity.

3.3. Out-of-plane response

The force-displacement curves for each group of walls tested in bending-parallel (Group BPR) are plotted in Fig. 14, whilst the main test results are summarised in Table 3. Note that the individual specimen response is shown with grey lines, while the black lines correspond to the average response from the specimens in each figure panel. The post-peak response is plotted up to a drop of 20 % of the peak axial force. The ultimate (peak) force (F_u) and displacement (δ_u) attained during testing, and stiffness (K_{x1}), determined at a range of 0–1/3 of the peak force, are presented in Table 3, along with the summarised statistics for each group of specimens. The displacement δ_u is the corrected mid-span displacement, after accounting for the relative displacement at the supports.

As shown from the test curves in Fig. 14, the TRM-strengthened walls exhibit significantly higher resistance, up to about 18 times higher than their URM counterparts (BPR0), on average. A comparison of the response of walls with one (BPR1) and two layers of mesh (BPR2) shows that the force and deformation capacity is nearly doubled when two mesh layers are provided. On the other hand, URM walls demonstrate poor performance, reaching ultimate forces of only about 1.24 kN. The average ultimate displacement is also considerably lower than the

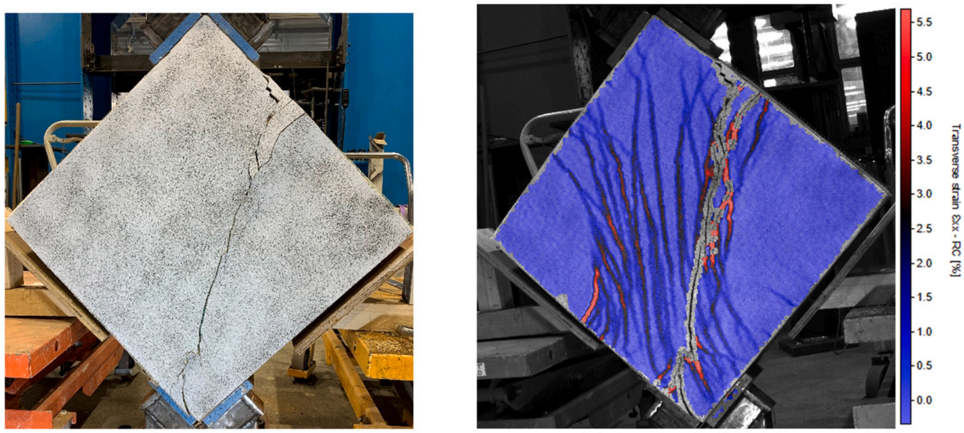

(a) (b)

Fig. 12. Failure of Wall D2c (Group D2): (a) crack pattern, and (b) strain map from DIC. Red colour indicates cracking or high strain concentration, whilst blue colour indicates low strain levels.

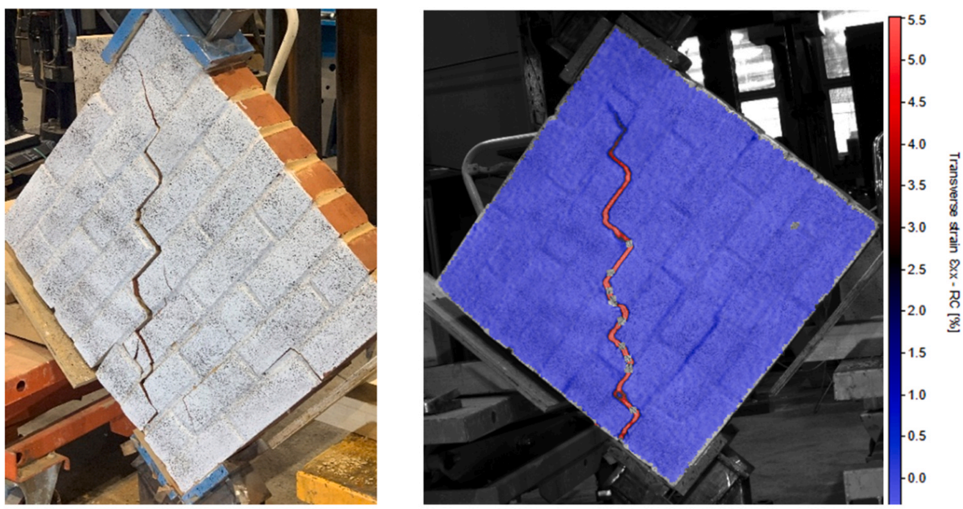

(a) (b)

Fig. 13. Failure of Wall D0a (Group D0): (a) crack pattern, and (b) strain map from DIC. Red colour indicates cracking or high strain concentration, whilst blue colour indicates low strain levels.

corresponding displacement for strengthened walls. These results highlight the benefits of using TRMs in improving the bending performance of existing masonry elements, both in terms of ultimate force and ductility. In addition, the stiffness of the walls is significantly enhanced when textile meshes are employed, as indicated by the higher stiffness of TRM-strengthened walls versus URM counterparts.

Fig. 15 shows the force-displacement curves of walls tested in bending-perpendicular (Group BPP), where the individual specimen response is plotted in grey and the average response in black. Similar to the bending-parallel case, the response is plotted up to a force drop of 20 % from the peak. Table 4 provides the ultimate force and displacement (F_u, δ_u), and stiffness (K_{x2}), determined at a range of 0–1/3 of the peak force, along with the summarised statistics for each group of walls. The ultimate force of TRM-strengthened specimens tested in bending parallel is very similar to the corresponding force of walls tested in bending perpendicular, suggesting that the presence of mesh reinforcement is the most significant parameter in determining the failure of walls in bending, rather than the brick arrangement.

When one (BPP1) or two (BPP2) mesh layers are employed, the formation of cracks is delayed, and when these are formed, they mostly follow a straight line on the surface of the specimens, regardless of the mortar joint paths. On the other hand, the capacity of URM walls (BPP0) is nearly tripled in the bending perpendicular tests compared to the corresponding bending parallel tests (BPR0). Due to the brick arrangement in the former case, the mortar joints along the width of the specimens do not follow a straight line, thus resulting in a longer path of cracks at failure, as discussed below. Therefore, in BPP tests of walls with no mesh, more energy is required for the cracks to be formed compared to BPR tests, and hence, higher ultimate force is attained. Similar to the observations made in BPR specimens, the stiffness is higher for TRM-strengthened walls in comparison with the URM elements.

Figs. 16 and 17 depict the crack patterns and strain maps at failure (after the peak load) from DIC for Specimens BPR2a and BPP2a, selected to demonstrate the failure mode of TRM-strengthened walls tested in the two arrangements. In BPR2a, the failure occurs with two horizontal cracks that are formed at the points of load application, resulting in the detachment of the outer part of the overlay mortar between these cracks.

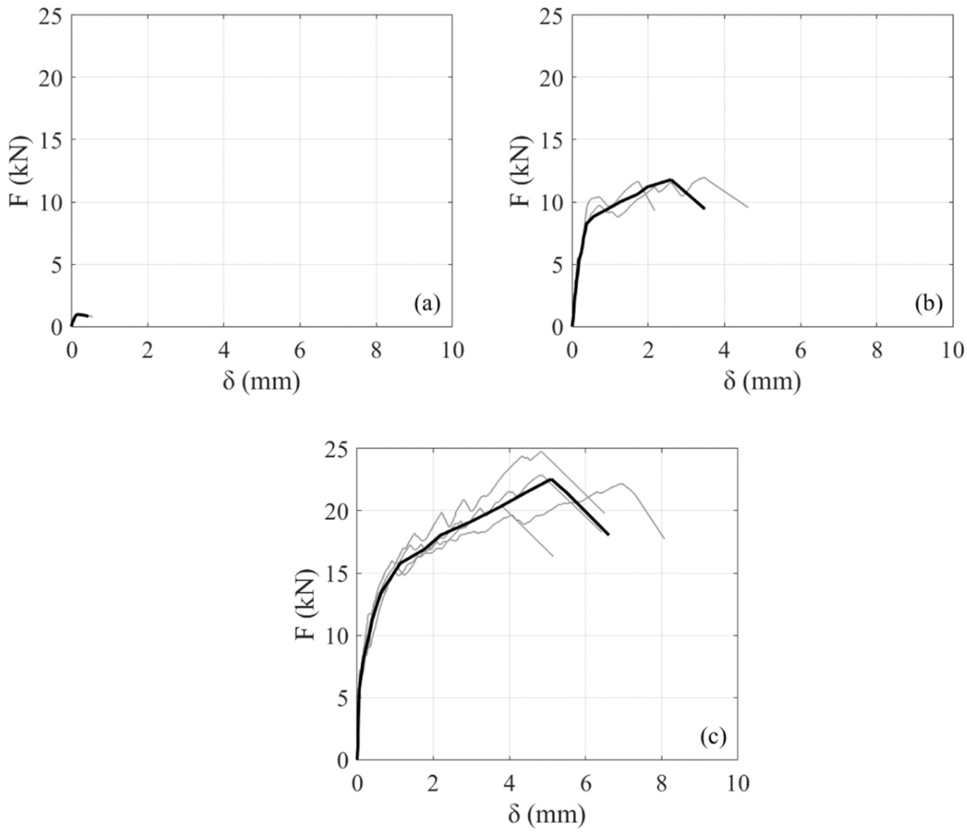

Fig. 14. Force-displacement curves of walls tested in bending parallel: (a) Group BPR0, (b) Group BPR1, and (c) Group BPR2. Black lines refer to the mean curves and grey lines indicate individual specimens.

Note that the detachment of the TRM overlay in Specimen BPR2a occurred after the end of the test, due to the formation of two horizontal cracks at failure, while during testing there was sufficient cohesion between the textile and the substrate. In the rest of the TRM-strengthened walls, with one or two layers of mesh, one horizontal crack was observed at failure, as shown for Specimen BPP2a in Fig. 17 and Specimens BPR2b and BPR1a in Fig. 18. The critical crack was formed through a mortar joint, at any location between the load application points, where the bending moment was maximised. In fact, multiple horizontal cracks were formed, until one of those opened abruptly, signalising the failure. Hence, the crack pattern was similar for all strengthened walls tested in bending.

A single crack at failure was observed in walls that had no mesh reinforcement (i.e., URM walls). In the case of URM BPR testing (Fig. 19), this passed through a mortar joint between the load application points. However, for URM BPP walls, the critical crack followed the mortar joints line, thus deviating significantly from the horizontal direction, as shown in Fig. 20. Hence, based on these observations, the failure crack pattern of walls tested in bending perpendicular depends on whether they are strengthened or not.

4. Analytical modelling

In this section, the test results are compared to analytical predictions, based on codified and other proposed approaches. In particular, American [40] and European [57,58] standards are compared, whilst improved models are also developed, aiming at ensuring more accurate estimates of shear and bending capacities, based on experimental data.

In addition to the experiments carried out in this investigation, a database with in-plane and out-of-plane tests on TRM-strengthened masonry from the literature is also collated. With respect to the TRM strengthening system, only glass, carbon, or basalt fibre reinforcing mesh were considered, as these materials exhibit comparable performance. In addition, only studies that reported material tests on mortars were included in the database. The main characteristics of the collated diagonal compression tests [18,26,48,59] and bending tests [26,60,61] are given in Tables 5 and 6, respectively. The values E_f and ε_{fu} in Tables 5 and 6 are taken from manufacturer data sheets, or, if not provided, from tests on the textile grid.

The in-plane and out-of-plane capacity of URM or TRM-strengthened masonry walls may be evaluated as a function of key geometric and mechanical properties of the masonry and TRM system. The main assumptions adopted in the analytical models presented in detail below are as follows: (i) plane sections remain plane during loading, (ii) the tensile strengths of masonry and overlay mortar are ignored in textile-reinforced masonry, and only the textile fibres are assumed to contribute in tension, (iii) the compressive strength of the fibres is neglected, (iv) perfect bond is assumed between the TRM and the masonry, thus ensuring strain compatibility, and (v) no end-debonding mechanism occurs.

4.1. In-plane response

The shear capacity of strengthened masonry can be estimated as the sum of the contributions from the URM and the TRM system. The focus herein is on the latter, in order to assess the efficiency of TRM as a strengthening option. TRM-specific expressions given in codes, as well as a recently proposed approach, are reviewed below.

4.1.1. American code

According to the North American code ACI 549.6 [40], the shear capacity enhancement due to TRM may be estimated from Eq. 3.

$$V_{t,ACI} = n_s A_f E_f \varepsilon_{fd} \tag{3}$$

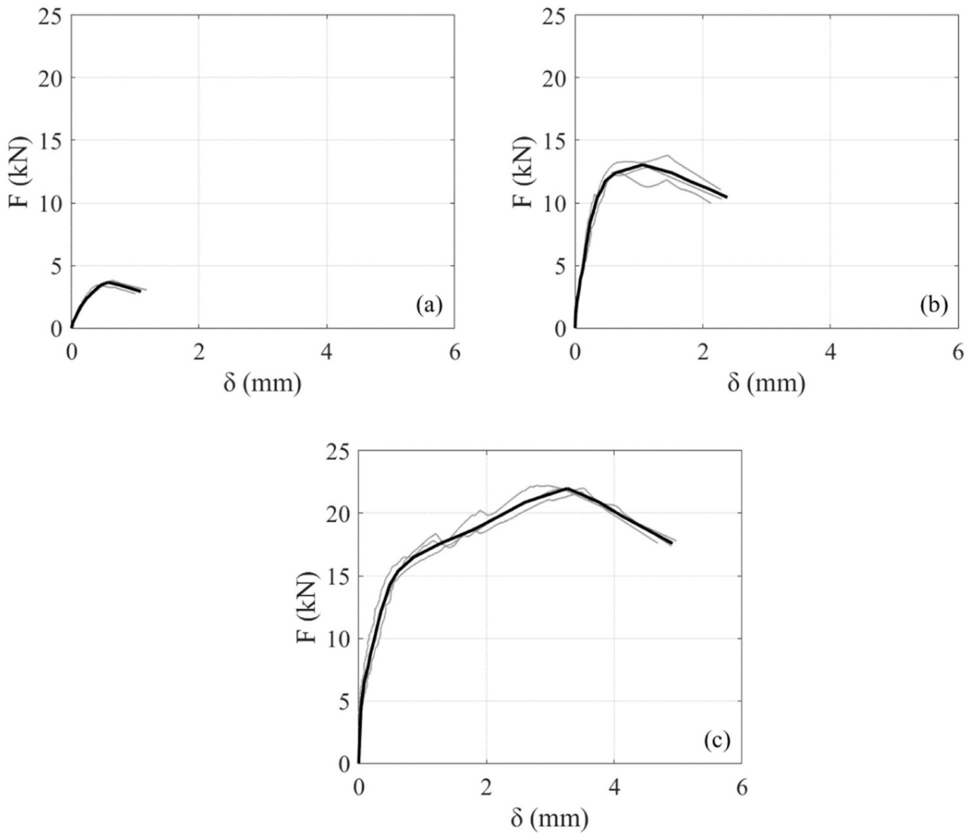

Fig. 15. Force-displacement curves of walls tested in bending perpendicular: (a) Group BPP0, (b) Group BPP1, and (c) Group BPP2. Black lines refer to the mean curves and grey lines indicate individual specimens.

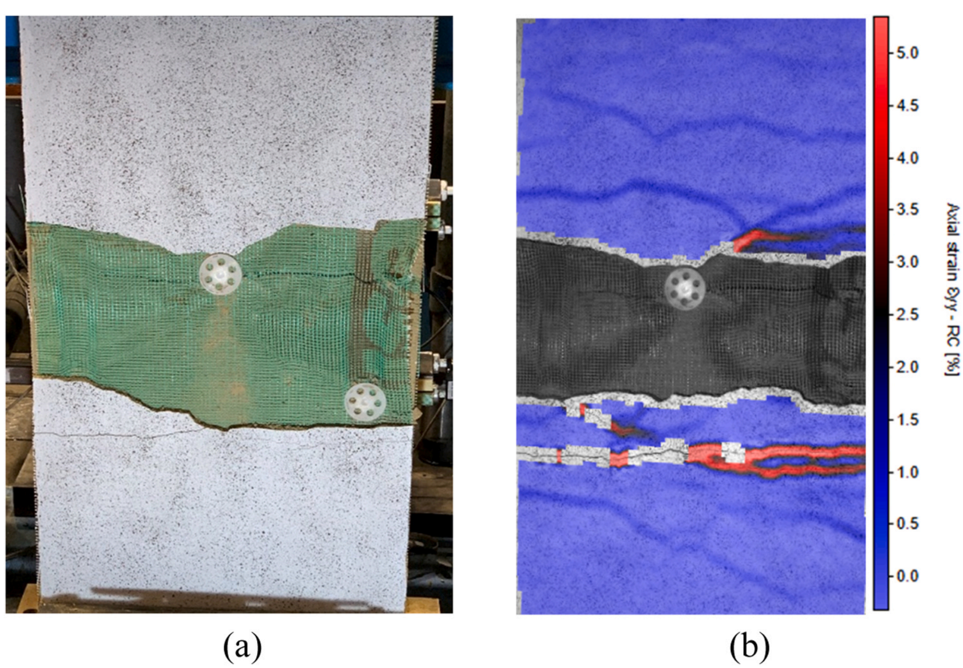

Fig. 16. Failure of Wall BPR2a (Group BPR2): (a) crack pattern, and (b) strain map from DIC. Red colour indicates cracking or high strain concentration, whilst blue colour indicates low strain levels.

where n_s is the number of sides of the wall that are strengthened; A_f is the shear-effective area of the fabric reinforcement per side; E_f is the cracked TRM stiffness; ε_{fd} is the design axial fibre strain.

The design axial fibre strain is limited to $\varepsilon_{fd} = 0.004$, unless specific experimental evidence supports the adoption of a higher limit. In this study, the code-specified limit of 0.004 is adopted for the axial fibre strain. Also, due to the lack of test data on TRM coupons in some of the

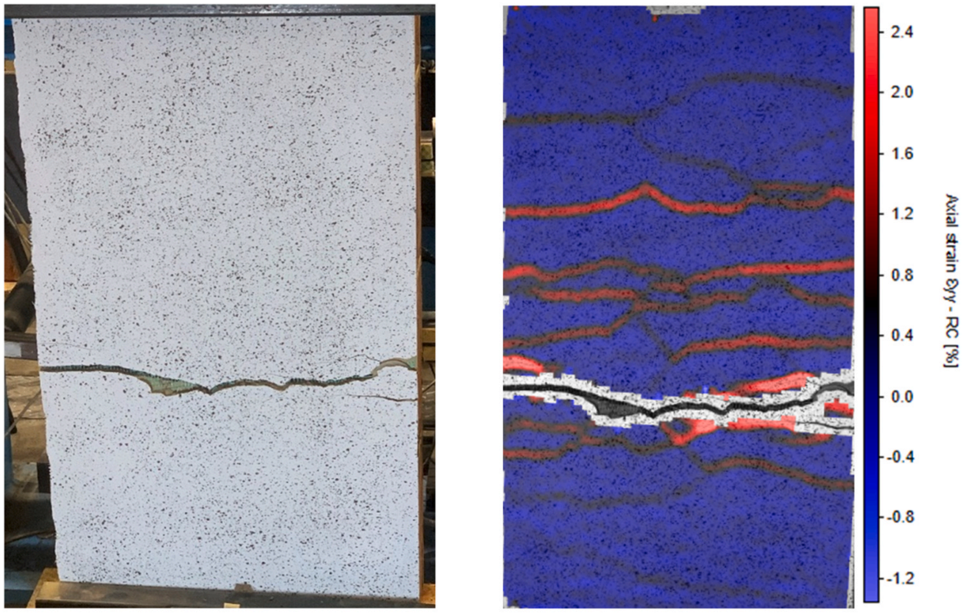

(a) (b)

Fig. 17. Failure of Wall BPP2a (Group BPP2): (a) crack pattern, and (b) strain map from DIC. Red colour indicates cracking or high strain concentration, whilst blue colour indicates low strain levels.

(a) (b)

Fig. 18. Failure of: (a) Wall BPR2b (Group BPR2), and (b) Wall BPR1a (Group BPR1).

studies in the collated database, the elastic modulus of the mesh grid is employed for estimating the ACI-based shear capacity enhancement due to TRM. Although this is not consistent with the code requirements, as the aim of this study is to compare design-oriented predictive expressions, the capacity predictions were based on manufacturer-provided properties and pre-determined limits of failure strains, rather than values obtained from testing (such as the cracked TRM stiffness that is prescribed in the ACI model). Note that the design lateral capacity of TRM-strengthened walls may be estimated as the sum of the TRM expression and the URM capacity (which is the minimum of the in-plane diagonal tension cracking and bed joint sliding capacity) and should not exceed the toe crushing capacity of the wall.

4.1.2. Italian code

The Italian Code CNR-DT 215 [57] provides Eq. 4 below for the TRM contribution to shear resistance.

$$V_{t,CNR} = n_s n_f t_{eff} l_f E_f \alpha_t \varepsilon_{fd} \quad (4)$$

where n_f is the total number of layers on each side; t_{eff} is the equivalent thickness of a fibre layer; l_f is the design dimension of the reinforcement perpendicular to the shear force (which typically covers the full length of the wall); E_f is the fibre elastic modulus; $\alpha_t = 0.8$ is a reduction factor that considers the reduction in the fibres tensile strength when they are loaded in shear.

Eq. 4 is similar to the expression suggested in ACI 549.6 (i.e. Eq. 3), considering that the product $n_f t_{eff} l_f$ represents the total area of the fibres per side (A_f). Although the recommended ultimate strain differs from that used in the American code, for the purpose of comparisons in this paper the same design strain limit of 0.004 is adopted in the Italian code provisions.

4.1.3. Proposed approach

Recently, Elghazouli et al. [48] proposed an improved approach to estimate the shear capacity of TRM-strengthened walls as the sum of contributions from the URM, the textile mesh, and the mortar overlay. The basic principles of this model are illustrated in Fig. 21. The shear force due to the mortar overlay and the fibres are noted in the figure, for a doubly reinforced masonry panel. Accordingly, the TRM contribution can be determined from Eq. 5.

$$V_{tr} = n_s A_f E_f \varepsilon_{fu} + \frac{n_s t_r l}{b} f_{t,r} \quad (5)$$

where ε_{fu} is the strain at failure (obtained from tests); t_r is the thickness of overlay mortar layer per side of the wall; b is a correction factor for the shear stress distribution in the middle section of the wall, defined in Eurocode 8 [62]; $f_{t,r} = 0.1 f_r$ is the tensile strength of the overlay mortar (equal to 10 % of the compressive overlay mortar strength f_r).

Note that the strain at failure may be obtained from TRM coupon tests, while the tensile strength of the mortar overlay may be estimated conservatively as 10 % of its compressive strength ($f_{t,r} = 0.1 f_r$) [55].

This model also incorporates the crushing strength, given in Eq. 6, which limits the ultimate shear strength capacity.

$$V_{sc} = 0.25 \beta_{sc} f_m l t \quad (6)$$

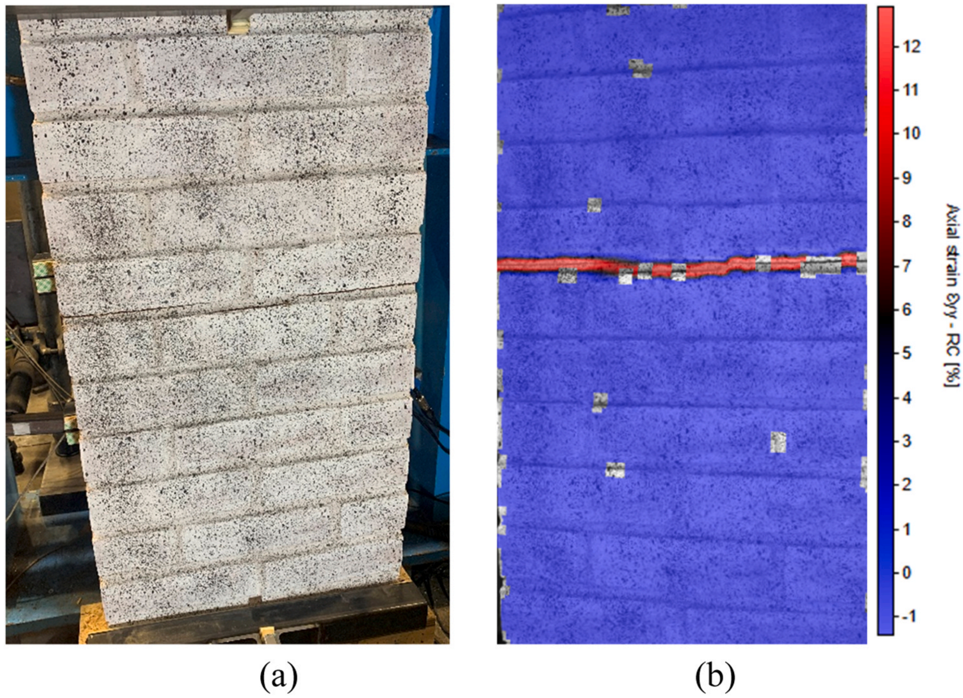

Fig. 19. Failure of Wall BPR0b (Group BPR0): (a) crack pattern, and (b) strain map from DIC. Red colour indicates cracking or high strain concentration, whilst blue colour indicates low strain levels.

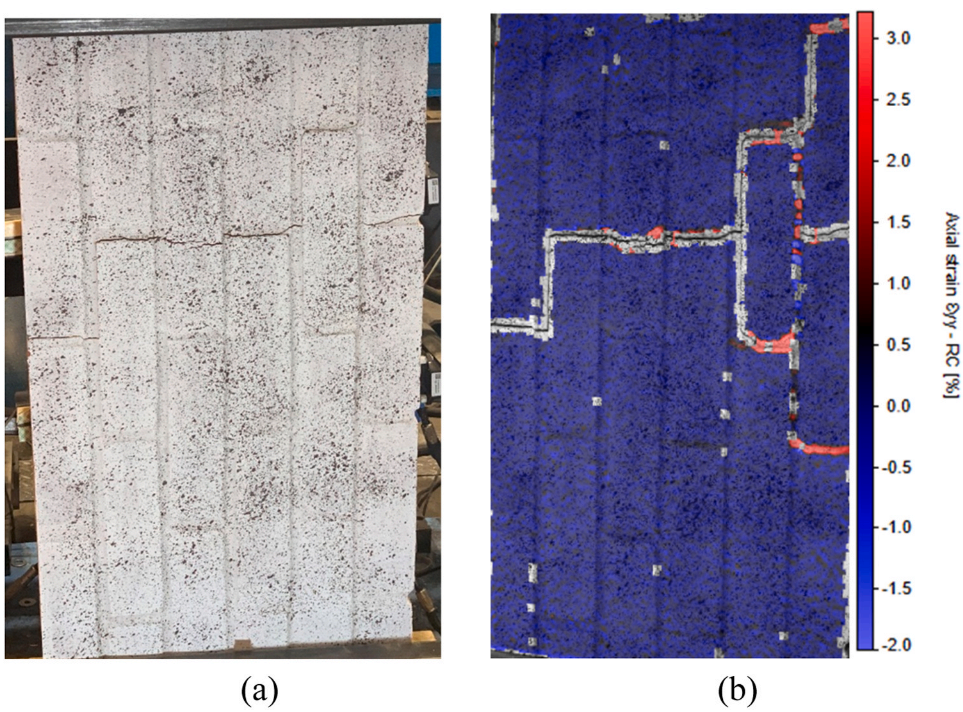

Fig. 20. Failure of Wall BPP0a (Group BPP0): (a) crack pattern, and (b) strain map from DIC. Red colour indicates cracking or high strain concentration, whilst blue colour indicates low strain levels.

The factor β_{sc} accounts for the confinement effect due to the TRM and typically varies between 1.15 and 1.20 for cohesive brittle materials [63]. A value of 1.15 is adopted in this study.

To facilitate the use of this model in the design, instead of using experimental values for the strain of the fibre mesh at failure, a recommended value for ε_{fu} is derived herein, based on the test results included in both the shear and bending databases (Tables 5 and 6). This is given in Eq. 7 and is selected so that the average experimental-to-predicted shear and moment capacity ratio is as close to unity as possible, considering all tests in the shear and bending database, respectively. Note that the studies in Tables 5 and 6 use coated glass mesh for the TRM strengthened masonry, and the proposed limit is not appropriate when uncoated textiles are employed. Also, the proposed strain limit may be unconservative when a single mesh layer is added

Table 5
Database of TRM-strengthened diagonal compression tests.

ID	Reference	n_f (-)	n_s (-)	Textile	E_f (GPa)	ε_{fu} (%)	h (mm)	l (mm)	t (mm)	f_m (MPa)	$V_{\exp}$ (kN)	$V_{t,\exp}$ (kN)	$V_{t,ACI}$ (kN)	$V_{t,CNR}$ (kN)	V_{tr} (kN)
D1a	This study	1	2	Glass	72.00	2.70[1]	688	688	125	6.35	170.35	120.52	12.29	9.83	71.74
D1b	This study	1	2	Glass	72.00	2.70[1]	688	688	125	6.35	178.84	129.01	12.29	9.83	67.06
D1c	This study	1	2	Glass	72.00	2.70[1]	688	688	125	6.35	173.38	123.55	12.29	9.83	75.35
D2a	This study	2	2	Glass	72.00	2.70[1]	688	688	125	6.35	203.31	153.47	24.58	19.66	129.05
D2b	This study	2	2	Glass	72.00	2.70[1]	688	688	125	6.35	194.97	145.13	24.58	19.66	123.39
D2c	This study	2	2	Glass	72.00	2.70[1]	688	688	125	6.35	190.56	140.72	24.58	19.66	123.06
DC-L1D-D1	[48]	1	2	Glass	72.00	2.70	710	710	110	5.50	143.58	66.75	5.50	4.40	66.11
DC-L1D-D2	[48]	1	2	Glass	72.00	2.70	710	710	110	5.50	138.70	61.87	5.50	4.40	66.11
DC-L1D-D3	[48]	1	2	Glass	72.00	2.70	710	710	110	5.50	168.89	92.05	5.50	4.40	66.11
DC-L1S-D1	[48]	1	1	Glass	72.00	2.70	710	710	110	6.10	126.05	49.22	2.75	2.20	28.52
DC-L1S-D2	[48]	1	1	Glass	72.00	2.70	710	710	110	6.10	112.85	36.01	2.75	2.20	28.52
DC-L1S-D3	[48]	1	1	Glass	72.00	2.70	710	710	110	6.10	125.75	48.92	2.75	2.20	28.52
DC-L2D-D1	[48]	2	2	Glass	72.00	2.70	710	710	110	6.20	153.40	76.57	10.99	8.79	95.67
DC-L2D-D2	[48]	2	2	Glass	72.00	2.70	710	710	110	6.20	162.80	85.96	10.99	8.79	95.67
DC-L2D-D3	[48]	2	2	Glass	72.00	2.70	710	710	110	6.20	165.46	88.63	10.99	8.79	95.67
TD1_R	[26]	1	2	Glass	67.00[2]	1.93[2]	1200	1200	250	3.28	213.58	128.01	18.80	15.04	143.29
TD2_R	[26]	1	2	Glass	67.00[2]	1.93[2]	1200	1200	250	3.28	248.89	163.32	18.80	15.04	143.29
TD3_R	[26]	1	2	Glass	67.00[2]	1.93[2]	1200	1200	250	3.28	223.68	138.11	18.80	15.04	143.29
MD1_R	[26]	1	2	Glass	67.00[2]	1.93[2]	1200	1200	250	7.89	509.89	113.39	18.80	15.04	143.29
MD2_R	[26]	1	2	Glass	67.00[2]	1.93[2]	1200	1200	250	7.89	586.55	190.05	18.80	15.04	143.29
MD3_R	[26]	1	2	Glass	67.00[2]	1.93[2]	1200	1200	250	7.89	482.15	85.65	18.80	15.04	143.29
PS1	[59]	2	2	Glass	72.00	1.78	1030	1030	250	2.30	196.40	107.38	46.08	36.86	183.89
PS2	[59]	2	2	Glass	72.00	1.78	1030	1030	250	2.30	234.30	145.28	46.08	36.86	183.89
PS3	[59]	1	2	Glass	72.00	1.78	1030	1030	250	2.30	207.90	118.88	23.04	18.43	126.78
PS4	[59]	1	2	Glass	72.00	1.78	1030	1030	250	2.30	154.70	65.68	23.04	18.43	126.78
PT1	[59]	2	1	Glass	72.00	1.78	1030	1030	250	2.30	128.20	39.18	23.04	18.43	126.78
PT2	[59]	2	1	Glass	72.00	1.78	1030	1030	250	2.30	168.10	79.08	23.04	18.43	126.78
PT3	[59]	1	1	Glass	72.00	1.78	1030	1030	250	2.30	181.80	92.78	11.52	9.22	63.39
PT4	[59]	1	1	Glass	72.00	1.78	1030	1030	250	2.30	124.40	35.38	11.52	9.22	63.39
PR1	[18]	1	1	Glass	72.00	1.77	1230	1230	310	1.95	242.66	122.23	11.52	9.22	60.85
PR2	[18]	1	1	Glass	72.00	1.77	1230	1230	310	1.95	221.09	100.66	11.52	9.22	60.85
PRR1	[18]	1	2	Glass	72.00	1.77	1230	1230	310	1.95	382.86	262.43	23.04	18.43	121.69
PRR2	[18]	1	2	Glass	72.00	1.77	1230	1230	310	1.95	366.68	246.25	23.04	18.43	121.69

[1] lowest specified elongation in the datasheet [39] (i.e., lateral elongation)
[2] data from tensile tests on grid

with properties similar to those of the mesh materials used in this paper. In the method presented herein, referred to as the proposed approach, the TRM contribution to the shear capacity may be estimated from Eq. 6, while the moment capacity of TRM-strengthened masonry may be determined from Eqs. 28–36 presented in Section 4.2.4, using the strain at failure from Eq. 7 in both cases.

$$\varepsilon_{fu} = 0.018 \tag{7}$$

4.1.4. Comparative assessments

The TRM contribution in shear capacity from tests carried out both in this study and previous tests included in the collated database (see Table 5), is compared to analytical predictions based on each of the above-mentioned methods in Fig. 22. The average and standard deviation of the experimental-to-predicted shear capacity ratios are noted at each panel. Current codes tend to highly underestimate the TRM contribution, providing overly conservative estimates. It is noteworthy that not only are the average values of the experimental-to-predicted shear capacity ratios much larger than one (9.49 with the ACI 549.6 and 11.86 with the CNR-DT 215), but all individual capacity ratios also exceed unity, implying that the predictions are conservative for every test included in the database. In contrast, when the proposed approach is employed, the data points are symmetrically distributed around the diagonal line, exhibiting a significant reduction in their average (1.30) and dispersion (0.45). The conservatism involved in current standards can be attributed to the adoption of a fixed fibre strain limit ($\varepsilon_{fd} = 0.004$), as suggested in ACI 549.6.

To investigate the effect of various parameters included in the proposed model, the shear strength (computed based on Eq. 5) normalised to the effective thickness (τ/t_{eff}) is plotted against the masonry compressive strength (f_m) in Fig. 23. A 1000 × 1000 × 300 mm glass fibre ($E_f = 72GPa$, $\varepsilon_{fu} = 0.018$) reinforced masonry wall is considered as the reference case in Fig. 23a, assuming an effective fibre thickness (t_{eff}) of 0.04 mm and overlay mortar compressive strength (f_r) equal to 30 MPa. Variations of this wall, considering increased section thickness ($t = 600mm$) and applied precompression ($\sigma_0 = 0.3\ MPa$) are presented in Figs. 23b and 23c, respectively. The lighter blue regions indicate the shear resistance of URM and masonry with mortar overlays on both sides, while the darker coloured contours correspond to TRM-strengthened masonry with 1–4 layers applied symmetrically on both sides of the panels. Assuming that diagonal cracking governs the response, the URM shear resistance was evaluated from Eq. 8 [62], adopting Eq. 9 [48] for the diagonal tensile strength of masonry f_t.

$$V_m = \frac{lt}{b} f_t \sqrt{1 + \frac{\sigma_0}{f_t}} \tag{8}$$

Table 6
Database of TRM-strengthened bending tests.

ID	Reference	n_f (-)	n_s (-)	Textile	E_f (GPa)	ε_{fu} (%)	h (mm)	l (mm)	t (mm)	σ_0 (MPa)	f_m (MPa)	M_{exp} (kNm)	M_{ACI} (kNm)	M_{CNR} (kNm)	M_{EC} (kNm)	M (kNm)
BPR2a	This study	2	2	Glass	72.00	2.70[1]	917	461	142	0.00	6.84	3.49	3.37	3.40	3.41	4.57
BPR2b	This study	2	2	Glass	72.00	2.70[1]	918	459	138	0.00	6.84	3.80	3.26	3.28	3.30	4.42
BPR2c	This study	2	2	Glass	72.00	2.70[1]	919	460	138	0.00	6.84	3.51	3.26	3.29	3.30	4.44
BPR2d	This study	2	2	Glass	72.00	2.70[1]	914	458	135	0.00	6.84	3.11	3.18	3.20	3.22	4.34
BPR1a	This study	1	2	Glass	72.00	2.70[1]	915	460	133	0.00	6.84	1.78	1.60	1.61	1.61	2.22
BPR1b	This study	1	2	Glass	72.00	2.70[1]	915	454	136	0.00	6.84	1.84	1.62	1.62	1.63	2.22
BPR1c	This study	1	2	Glass	72.00	2.70[1]	915	460	128	0.00	6.84	1.46	1.54	1.55	1.55	2.15
BPP2a	This study	2	2	Glass	72.00	2.70[1]	932	451	142	0.00	6.99	3.43	3.30	3.32	3.34	4.55
BPP2b	This study	2	2	Glass	72.00	2.70[1]	932	450	140	0.00	6.99	3.39	3.24	3.27	3.28	4.41
BPP2c	This study	2	2	Glass	72.00	2.70[1]	931	449	138	0.00	6.99	3.45	3.19	3.21	3.23	4.33
BPP1a	This study	1	2	Glass	72.00	2.70[1]	935	447	137	0.00	6.99	2.01	1.61	1.61	1.62	2.22
BPP1b	This study	1	2	Glass	72.00	2.70[1]	933	449	138	0.00	6.99	1.92	1.63	1.63	1.64	2.24
BPP1c	This study	1	2	Glass	72.00	2.70[1]	934	447	139	0.00	6.99	2.12	1.63	1.63	1.64	2.27
GFRCM_01	[60]	1	1	Glass	65.00	1.20	2700	1200	250	0.20	3.73	22.38	13.54	13.62	13.69	19.94
GFRCM_02	[60]	1	1	Glass	70.00	1.50	2700	1200	250	0.20	3.73	18.97	13.37	13.45	13.52	19.70
GFRCM_02	[61]	1	1	Glass	70.00	2.90	2700	1200	250	0.20	3.73	19.03	9.34	9.36	9.41	13.77
GFRCM_03	[61]	1	1	Glass	72.00	1.80	2700	1200	250	0.20	3.73	18.47	8.86	8.88	8.92	13.06
TB1_R	[26]	1	2	Glass	67.00[2]	1.93[2]	1200	800	310	0.00	3.28	12.15	6.15	6.16	6.18	9.05
TB2_R	[26]	1	2	Glass	67.00[2]	1.93[2]	1200	800	310	0.00	3.28	10.94	6.15	6.16	6.18	9.05
TB3_R	[26]	1	2	Glass	67.00[2]	1.93[2]	1200	800	310	0.00	3.28	11.60	6.15	6.16	6.18	9.05
MB1_R	[26]	1	2	Glass	67.00[2]	1.93[2]	1200	800	310	0.00	7.89	11.82	6.21	6.22	6.23	9.48
MB2_R	[26]	1	2	Glass	67.00[2]	1.93[2]	1200	800	310	0.00	7.89	12.63	6.21	6.22	6.23	9.48
MB3_R	[26]	1	2	Glass	67.00[2]	1.93[2]	1200	800	310	0.00	7.89	10.30	6.21	6.22	6.23	9.48

[1] lowest specified elongation in the datasheet [39] (i.e., lateral elongation)
[2] data from tensile tests on grid

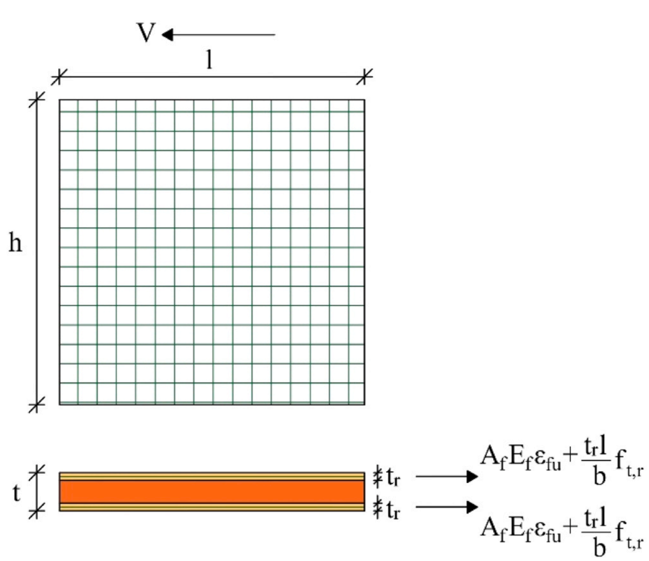

Fig. 21. Shear forces due to the contribution of the overlay mortar and textile for a masonry panel subjected to shear loading, according to the proposed approach.

$$f_t = 0.0163 f_m^{\ 1.88} \tag{9}$$

where σ_0 is the precompression stress.

The possible failure modes of TRM-strengthened walls are also shown in Fig. 23. The blue regions and dashed blue lines refer to failure due to rupture of the fibres, which is estimated as the sum of the URM shear resistance (Eq. 8) and the TRM contribution (Eq. 5), while the red diagonal line corresponds to the crushing capacity of masonry (Eq. 6). The latter failure mode dominates for low-strength masonry, trimming the strength enhancement provided by each layer of reinforcement. Hence, adding more reinforcement layers improves the shear resistance only for masonry strength higher than the critical f_m level at which masonry crushing governs. This critical strength limit increases with increasing number of layers and increasing precompression, while it reduces as the section thickness increases.

It is worth noting that the contribution of each layer of reinforcement is the same and considerably larger than the strength enhancement due to the overlay mortar. This justifies the disregard of the overlay mortar in current codified approaches, as its effect is negligible compared to the influence of the mesh reinforcement. For the masonry wall considered herein, increased section thickness results in reduced fibre contribution. Applying initial precompression results in slightly enhanced capacities both for URM and TRM-strengthened masonry.

4.2. Out-of-plane response

The out-of-plane flexural capacity of strengthened masonry walls from this work and previous studies included in the database is

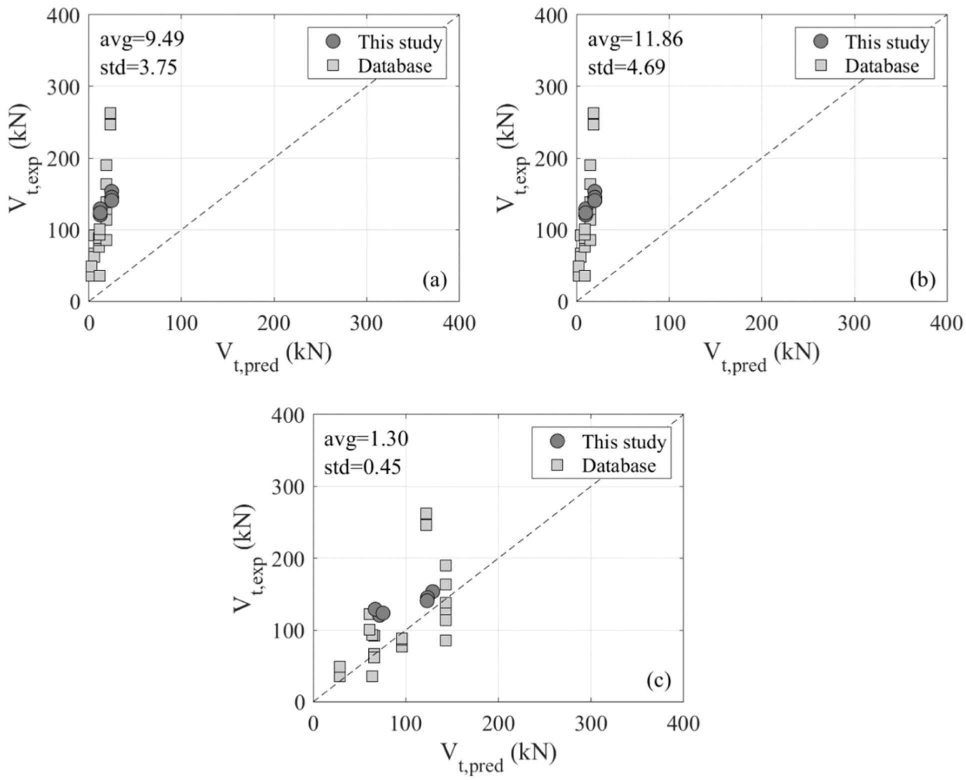

Fig. 22. Experimental against predicted TRM contribution to shear capacity based on: (a) ACI 549.6 [40], (b) CNR-DT 215 [57], and (c) proposed approach.

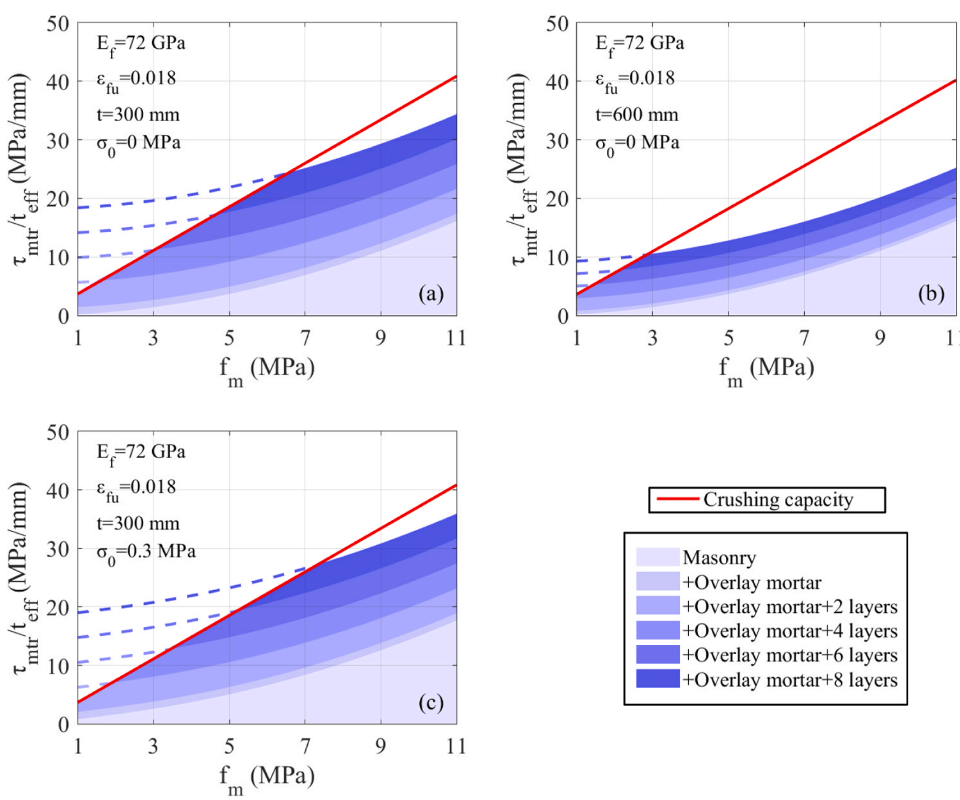

Fig. 23. (a) Normalised shear strength as a function of masonry compressive strength for a masonry wall, and effect of: (b) section thickness, and (c) precompression stress. Lighter blue colours correspond to URM, while darker colours indicate increased resistance due to overlay mortar and 1–4 layers of mesh reinforcement applied symmetrically on both sides of the walls. Blue lines indicate failure due to fibre rupture, while red line indicates failure due to crushing.

analytically evaluated in this section using the ACI 549.6 [40] and CNR-DT 215 [57] guidelines, as well as a European-based [58] and a new proposed approach.

4.2.1. American code

In addition to the assumptions mentioned earlier, the American code ACI 549.6 [40] also assumes that the contribution of the overlay mortar in compression can be disregarded when evaluating the out-of-plane resistance of TRM-strengthened masonry. Hence, only the masonry acts in compression, while the fibres in the reinforcement mesh provide the tensile resistance of the cross-section. A rectangular stress block is considered to simplify the parabolic stress-strain constitutive representation for masonry, with length βx_{ACI} and stress γf_m, where β, γ are stress block parameters, x_{ACI} is the neutral axis depth, and f_m is the masonry compressive strength. The stress-strain relationship of the fibres is assumed to be linear-elastic with a Young's modulus E_f, as provided by the manufacturer. The basic assumptions of the ACI 549.6 model are shown in Fig. 24, which illustrates the strain and stress distribution for a masonry panel, in addition to the forces acting on the section. An external axial force N is assumed.

Two modes of failure are distinguished, namely, masonry crushing and TRM rupture. The failure mode is identified by assuming that both the masonry and the TRM reach their ultimate strain simultaneously and comparing the value of the applied axial load to the total resistance from the masonry and the TRM. If the total tensile axial force in the cross-section exceeds the compressive axial force from the masonry, then masonry crushing governs. In contrast, if there is a compressive force surplus, then failure occurs by TRM rupture. Through strain compatibility and axial force equilibrium considerations, the depth to the neutral axis (x_{ACI}) and the extreme strain at fibres (ε_{fe}) and masonry (ε_{me}) may be evaluated from Eqs. 10–12, for the case of masonry crushing, and Eqs. 13–15 for TRM failure.

$$\gamma f_m \beta l {x_{ACI}}^2 + \left(A_f \varepsilon_{mu} E_f - N\right) x_{ACI} - A_f \varepsilon_{mu} E_f d = 0 \tag{10}$$

$$\varepsilon_{fe} = \frac{\varepsilon_{mu}(d - x_{ACI})}{x_{ACI}} < \varepsilon_{fu} \tag{11}$$

$$\varepsilon_{me} = \varepsilon_{mu} \tag{12}$$

$$x_{ACI} = \frac{N + A_f \varepsilon_{fu} E_f}{\gamma f_m \beta l} \tag{13}$$

$$\varepsilon_{fe} = \varepsilon_{fu} \tag{14}$$

$$\varepsilon_{me} = \frac{\varepsilon_{fu} x_{ACI}}{d - x_{ACI}} < \varepsilon_{mu} \tag{15}$$

According to ACI 549.6 [40], the stress block parameters are defined as $\beta = \gamma = 0.8$ for masonry crushing, and $\beta = \gamma = 0.7$ for TRM failure, while the ultimate masonry strain is, $\varepsilon_{mu} = 0.035$ and the ultimate fibre strain is $\varepsilon_{fu} = 0.012$. After obtaining the neutral axis depth, the moment capacity can be determined from Eq. 16.

$$M_{ACI} = 0.5 \gamma f_m \beta x_{ACI} l (d - \beta x_{ACI}) + 0.5 A_f \varepsilon_{fe} E_f d \tag{16}$$

4.2.2. Italian code

According to the Italian code CNR-DT 215 [57], the flexural capacity of TRM-strengthened masonry panels can be estimated based on the structural properties of the masonry and the textile. The stress-strain constitutive relationship for masonry is assumed as elastic-perfectly plastic, with the strength increasing linearly up to the design strain ε_{md}, then remaining constant and equal to the masonry strength f_m up to the ultimate strain ε_{mu}, and finally dropping to zero for larger strains.

Similar to the ACI guidelines, two modes of failure are also discerned in the Italian code. If failure at masonry occurs ($\varepsilon_m = \varepsilon_{mu}$), the neutral axis depth (x_{CNR}) and moment capacity (M_{CNR}) can be determined from Eqs. 17 and 18, respectively, by introducing the parameter k that represents the ratio of the design to the ultimate masonry strain, as shown in Eq. 19.

$$x_{CNR} = \frac{N - A_f \varepsilon_{mu} E_f + {A_f}^2 {\varepsilon_{mu}}^2 {E_f}^2 + N^2 - 2N A_f \varepsilon_{mu} E_f + 2(2-k) f_m l A_f \varepsilon_{mu} E_f d}{(2-k) f_m l} \tag{17}$$

$$M_{CNR} = A_f E_f \varepsilon_{mu}(d + 0.5 k x_{CNR} - 0.5 x_{CNR}) + f_m l k x^2 (0.25 - 0.083k) \tag{18}$$

$$k = \frac{\varepsilon_{md}}{\varepsilon_{mu}} \tag{19}$$

If the failure strain is reached at the fibres and the masonry is in the elastic range ($\varepsilon_m \le \varepsilon_{md}$), the neutral axis and moment capacity may be evaluated from Eqs. 20 and 21, respectively.

$$x_{CNR} = \frac{N + A_f \varepsilon_{fu} E_f}{0.5 f_m l} \tag{20}$$

$$M_{CNR} = A_f E_f \varepsilon_{fu} \left(d - \frac{x_{CNR}}{3}\right) \tag{21}$$

In case of fibre rupture while the masonry is in the plastic range ($\varepsilon_{md} < \varepsilon_m \le \varepsilon_{mu}$), the neutral axis and moment capacity are estimated from Eqs. 22 and 23, respectively, where the parameter k, introduced in Eq. 24, is the ratio of the design masonry strain to the ultimate fibre strain.

$$x_{CNR} = \frac{N + A_f \varepsilon_{fu} E_f + 0.5 k d f_m l}{(1 + 0.5k) f_m l} \tag{22}$$

$$M_{CNR} = A_f E_f \varepsilon_{fu}[(1 + 0.5k)d - 0.5(1+k)x_{CNR}] - 0.5 f_m l k (d - x_{CNR}) \left[(0.5 + \frac{k}{6}) x_{CNR} - \frac{k}{6} d\right] \tag{23}$$

$$k = \frac{\varepsilon_{md}}{\varepsilon_{fu}} \tag{24}$$

The strain limit for masonry crushing is defined as $\varepsilon_{mu} = 0.035$, while the ultimate fibre rupture limit ε_{fu} is the conventional strain limit $\varepsilon^{(a)}_{\mathrm{lim},conv}$ in the case of failure mechanisms due to intermediate debonding

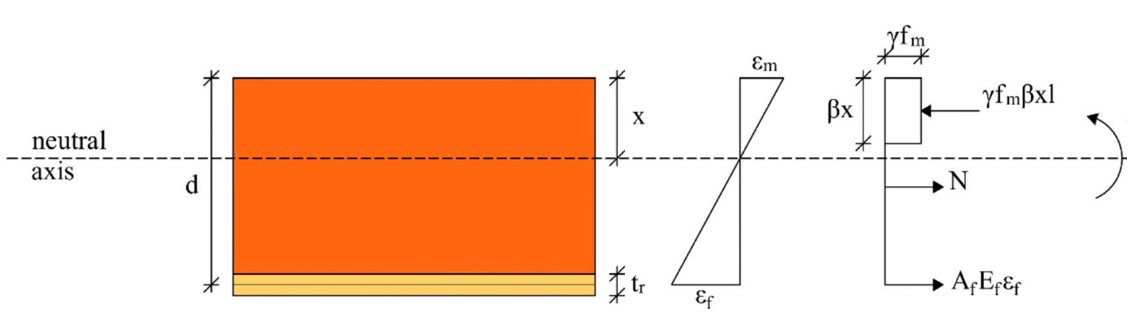

Fig. 24. Strain and stress distribution for a masonry panel subjected to bending and corresponding sectional forces, according to ACI 549.6 [40].

or the conventional strain limit $\varepsilon_{\lim,conv}$ in the case of end debonding [57]. In the absence of experimental data and to ensure that the results are comparable, the strain limit recommended by the American code (0.012) is also adopted in the Italian code provisions. The yield strain of masonry is taken as $\varepsilon_{md} = 0.001$, assuming a value for the masonry Young's Modulus of $E_m = 1000 f_m$, as suggested in Eurocode 6 [58].

4.2.3. European-based approach

In the absence of Eurocode-based provisions for TRM-strengthened masonry members, an approach based on Eurocode 6 [58], is introduced for the assessment of the out-of-plane strength of masonry walls. Specifically, Eurocode 6 [58] only provides guidelines for singly reinforced masonry with steel reinforcement. This can, however, be adapted for glass fibre reinforcement, adopting the strain limit of 0.012 proposed in the American code [40].

According to Eurocode 6 [58], a rectangular stress distribution is assumed to simplify the masonry response in compression, with strength f_m and length βx_{EC}, where β is a reduction factor of the neutral axis depth x_{EC}. It is also assumed that both the masonry and the fibres reach their ultimate strain simultaneously. The ultimate masonry strain is taken as $\varepsilon_{mu} = 0.035$, while the ultimate fibre strain is considered as $\varepsilon_{fu} = 0.012$, adopting the limit proposed in ACI 549.6 [40], due to the lack of European-based guidance.

The neutral axis and moment capacity can be evaluated from Eqs. 25 and 26. Note that these have been modified from the equations in Eurocode 6 [58] to include the axial force. However, they are only applicable for members strengthened on one side, disregarding any possible contribution of overlay mortar in compression for doubly reinforced masonry panels.

$$x_{EC} = \frac{N + A_f \varepsilon_{fu} E_f}{\beta f_m l} \tag{25}$$

$$M_{EC} = 0.5 N d \left(1 - \frac{N + A_f \varepsilon_{fu} E_f}{f_m l d}\right) + A_f E_f \varepsilon_{fu} d \left(1 - 0.5 \frac{N + A_f \varepsilon_{fu} E_f}{f_m l d}\right) \tag{26}$$

4.2.4. Proposed approach

An improved analytical approach for evaluating the flexural resistance of out-of-plane strengthened masonry walls is developed herein by accounting for the contribution of the overlay mortar in compression and adopting updated ultimate fibre strain limits for each TRM material type, as given in Eq. 7. In addition, the stress-strain relationship for masonry is simplified through a rectangular stress block with strength f_m and length βx, where β is a reduction factor of the neutral axis depth x. The overlay mortar is assumed to exhibit elastic-perfectly plastic response with elastic modulus E_r and strength f_r, obtained by fitting a bilinear curve to the experimental results. The fibres are assumed to be elastic with an elastic modulus E_f as given by the manufacturer. In Fig. 25, the assumed strain and stress distributions for a masonry panel in bending are depicted, along with the sectional forces.

Similar to the ACI 549.6 [40] and CNR-DT 215 [57] provisions, a distinction is made with respect to the failure mode. Assuming fibre rupture, the neutral axis depth and moment capacity are evaluated from Eqs. 27–30. The strain at the extreme masonry fibre is then evaluated from Eq. 31 and compared to the ultimate masonry strain ($\varepsilon_{mu} = 0.035$). If the ultimate strain limit is reached at the masonry, masonry crushing occurs, and the initial assumption of fibre rupture is invalid. In this case, the neutral axis and moment capacity may be computed from Eqs. 32–35, corresponding to failure due to masonry crushing.

$$\beta f_m b x^2 + [\beta f_m l (t_r - d) - t_r l E_r \varepsilon_{fu} - A_f E_f \varepsilon_{fu} - N] x + (N + A_f E_f \varepsilon_{fu})(d - t_r) - l t_r^2 E_r \varepsilon_{fu} = 0 \tag{27}$$

$$\varepsilon_r = \frac{\varepsilon_{fu}(x + t_r)}{d - x - t_r} \tag{28}$$

$$\sigma_r = \begin{cases} E_r \varepsilon_r, & \varepsilon_r < f_r / E_r \\ f_r, & \varepsilon_r \geq f_r / E_r \end{cases} \tag{29}$$

$$M = N(0.5d - 0.5\beta x - t_r) + A_f E_f \varepsilon_{fu}(d - 0.5\beta x - t_r) + \sigma_r l t_r (0.5\beta x + 0.5 t_r) \tag{30}$$

$$\varepsilon_{me} = \frac{\varepsilon_{fu} x}{d - x - t_r} \tag{31}$$

$$\beta f_m l x^2 + [t_r l E_r \varepsilon_{mu} + A_f E_f \varepsilon_{mu} + N] x + (N + A_f E_f \varepsilon_{mu})(t_r - d) + 0.5 l t_r^2 E_r \varepsilon_{mu} = 0 \tag{32}$$

$$\varepsilon_r = \frac{\varepsilon_{mu}(x + t_r)}{x} \tag{33}$$

$$M = N(0.5d - 0.5\beta x - t_r) + A_f E_f \varepsilon_{fe}(d - 0.5\beta x - t_r) + s_r l t_r (0.5\beta x + 0.5 t_r) \tag{34}$$

$$\varepsilon_{fe} = \frac{\varepsilon_{mu}(d - x - t_r)}{x} \tag{35}$$

4.2.5. Comparative assessments

The four approaches for estimating the out-of-plane moment capacity of TRM-strengthened masonry walls were applied to the bending tests carried out in this research, as well as various tests from the literature (see Table 6). The predicted moment capacities, as obtained using each approach and for each test, are plotted against the experimental results in Fig. 26, with the average and standard deviation of the experimental-to-predicted capacity ratios shown on the top left corner of each figure panel. The ACI 549.6 [40] and CNR-DT 215 [57] codes, as well as the European-based approach [58], result in very similar predictions, with an average of about 1.42 and a standard deviation of about 0.41. This highlights the significance of the ultimate fibre strain limit, which was defined as 0.012 in these approaches. These methods showed considerable discrepancy from the test results, as indicated by mean values not close to unity and the scatter of results around the

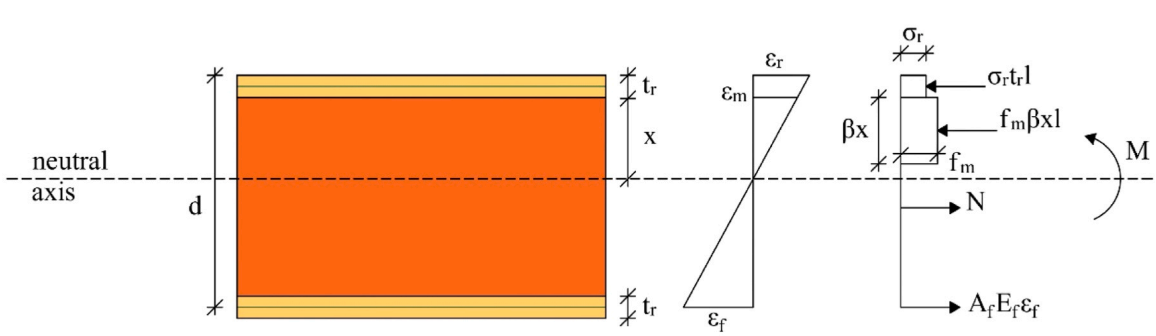

Fig. 25. Strain and stress distribution for a masonry panel subjected to bending and corresponding sectional forces, according to the proposed approach.

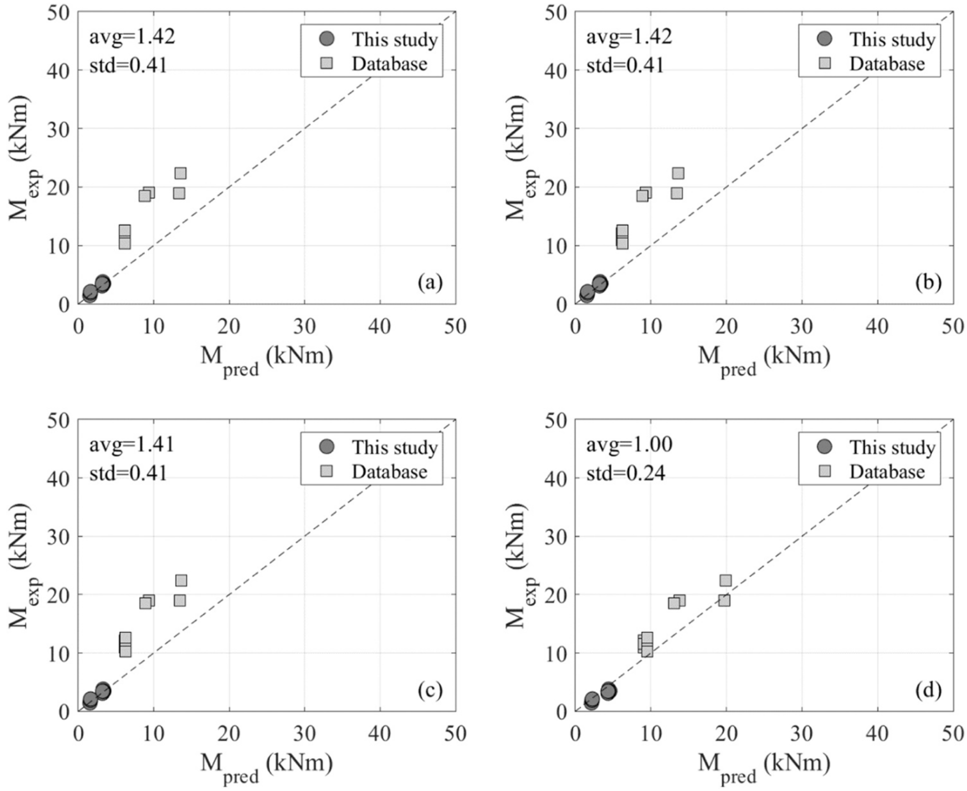

Fig. 26. Experimental against predicted moment capacity based on: (a) ACI 549.6 [40], (b) CNR-DT 215 [57], (c) Eurocode-based approach [58], and (d) proposed approach.

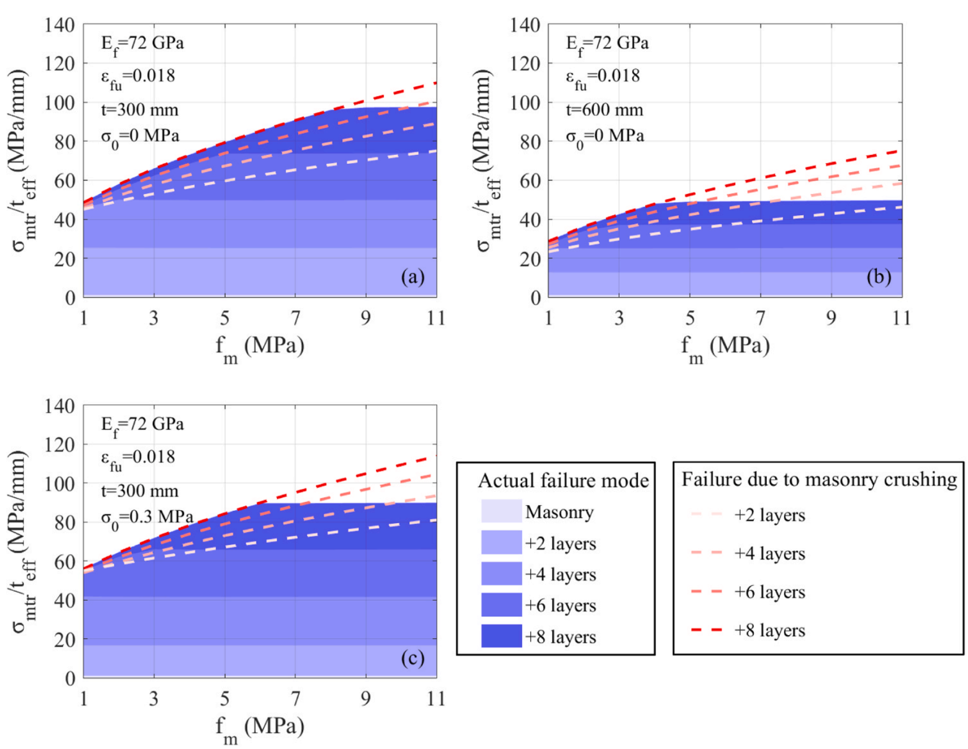

Fig. 27. (a) Normalised bending strength as a function of masonry compressive strength for a masonry wall, and effect of: (b) section thickness, and (c) pre-compression stress. Lighter blue colours correspond to URM, while darker colours indicate increased resistance due to 1–4 layers of mesh reinforcement applied symmetrically on both sides of the walls. Blue lines indicate the actual failure mode attained, while the red dashed lines indicate failure due to masonry crushing.

diagonal line. The most accurate estimates are obtained from the method proposed in this study, in which case the average experimental-to-predicted moment capacity ratio reaches unity, and the standard deviation is comparatively lower, at 0.24.

In Fig. 27, the bending strength, evaluated using the proposed approach (Eqs. 27–35) and normalised to the effective thickness (σ/t_{eff}), is plotted against the masonry compressive strength (f_m), for various configurations of URM or TRM-strengthened walls, in a similar format to Fig. 23. The same masonry wall that was used in Fig. 23 is also considered herein, with the same variation of properties in panels a-c. The contribution of mortar overlays in bending is negligible, as the flexural tensile strength of masonry ($f_x = 0.1MPa$, assuming lightweight lime-mortar and clay bricks and following guidance in Eurocode 6 [58]) is lower than the tensile strength of the overlay mortar ($f_{t,r} = 0.1f_r = 0.3MPa$, assuming a compressive strength of the overlay mortar $f_r = 30MPa$). Hence, the masonry contribution is critical and dictates the capacity of both URM and masonry with overlay mortar. Therefore, only URM and the contributions from mesh layers are shown in Fig. 27. The moment capacity of URM is estimated according to Eq. 36.

$$M_m = f_x \frac{lt^2}{6} \tag{36}$$

The blue contours show the actual failure mode attained at each level of f_m, while the red dashed lines indicate masonry crushing. Hence, in regions where the blue contours follow the red dashed lines, failure is due to masonry crushing, while fibre rupture occurs where the two diverge. Masonry crushing governs for low-strength masonry, while the critical strength limit that signalises the transition to fibre fracture failure increases as the number of layers increases. When fibre fracture governs, the capacity ultimately becomes independent of the masonry compressive strength.

Each panel in Fig. 27 corresponds to a specific combination of section thickness and precompression level. An increase in the section thickness is shown to reduce the capacity, shifting all contours at lower levels of normalised strength. A relatively smaller effect can be discerned with respect to the level of precompression.

5. Concluding remarks

In this paper, the in-plane and out-of-plane response of URM and TRM-strengthened masonry was assessed through a total of thirty-nine specimens tested in axial compression, diagonal compression, and bending with load application parallel and perpendicular to the bed joints. The masonry included hydraulic lime mortars and fired clay bricks, with properties selected to represent heritage structures in Historic Cairo. From the total number of tests, eighteen were strengthened with one or two layers of alkali age-resistant glass fibre mesh applied to each side and embedded in a cement-lime overlay mortar to ensure sufficient connection to the substrate. Additional material tests were carried out for the characterisation of bed joint mortars, overlay mortars, bricks, and TRM coupons.

The main conclusions from the experimental programme are outlined below.

- Overlay mortars showed, on average, about six times higher strength than the bed joint mortars. Bricks tested parallel to the bed face exhibited nearly twice the strength of those tested perpendicular to the bed face, which is attributed to their low aspect ratio and the resulting higher levels of confinement. Increased tensile strength and deformation at failure by factors of about 2.0 and 1.4, respectively were obtained for TRM coupons with two layers, compared to those with one mesh layer.
- The compressive strength of masonry wallettes varied in the range of 5.92–7.40 MPa. Their cracking pattern at failure showed two main vertical cracks on both sides, near the edge, that initiated from the bed joints and propagated through the height of the specimens.
- URM panels tested in diagonal compression failed in a brittle manner, due to a main critical stepped crack joining the edges of the top and bottom supports, reaching a shear strength of 0.44 MPa, on average. This increased to approximately 1.42 MPa for TRM-strengthened panels, in which a more ductile failure was achieved, involving the formation of multiple cracks. The TRM strengthening was shown to enhance the in-plane response of URM walls, yet an increase in mesh layers had a minimal influence on the shear resistance.
- The ultimate force of URM walls tested in bending depended on the brick arrangement, reaching a value of about 3.65 kN, on average, for loading perpendicular to the bed joints, while this reduced to only 1.24 kN when the loading was applied parallel to the bed joints. In contrast, the brick arrangement did not have a significant effect on the resistance of TRM specimens. Walls with one mesh layer, tested either in bending parallel or perpendicular, exhibited ultimate force of about 12.42 kN, while those strengthened with two mesh layers showed increased resistance, at 22.26 kN, on average. This distinct response of URM and TRM walls was also reflected in their crack patterns. For URM walls, the critical crack in bending parallel tests developed horizontally through a mortar joint located at the region of maximum bending moment, while in the bending-perpendicular tests, the critical crack diverted from the horizontal orientation, following the mortar joints path. TRM-strengthened walls typically failed with one horizontal crack close to mid-height, where the bending moment was maximum, for both the examined brick arrangements.

The test results from this investigation, along with a series of tests from the literature, were compared against existing and proposed analytical approaches for the design of TRM-strengthened walls in shear and bending. Expressions for the enhancement in shear resistance due to TRM strengthening given in the American (ACI 549.6) and the Italian (CNR-DT 215) codes, as well as an analytical approach that incorporates the fibre strain limit proposed in this work, were assessed against the test results. The American and Italian code predictions were shown to be grossly overconservative, mostly due to the associated low design fibre strain limit prescribed, whilst the proposed approach resulted in much closer shear capacity estimates to those obtained experimentally and with considerably lower standard deviation than for the code predictions. Sensitivity analyses based on the proposed approach revealed that the precompression stress was a secondary parameter.

The bending resistance of TRM-strengthened walls was evaluated as per the North American (ACI 549.6) and the Italian (CNR-DT 215) code, a European-based approach, and a proposed approach that considers the contribution of the mortar overlay in compression and a suggested fibre strain limit. Comparative assessments indicated that the American and Italian codes, as well as the European-based approach, resulted in overly conservative predictions of the bending moment. The proposed approach, on the other hand, provided a mean bending capacity estimate that was very close to the mean test values and with relatively low standard deviation compared to the code predictions. As for the in-plane response, using this proposed approach, it was shown that the initial precompression stress is of minor importance.

Overall, the proposed analytical approaches for determining the in-plane and out-of-plane strength provide close prediction of the experimental capacities from this study as well as those from a wider collated database of previous tests. They are therefore suitable for implementation in practical assessment and rehabilitation guidelines.

CRediT authorship contribution statement

D.V. Bompa: Writing – review & editing, Supervision, Methodology, Investigation, Formal analysis, Data curation, Conceptualization. **A. Y. Elghazouli:** Writing – review & editing, Supervision, Resources, Project administration, Methodology, Funding acquisition, Conceptualization.

M. Liapopoulou: Writing – original draft, Validation, Software, Methodology, Investigation, Formal analysis, Data curation, Conceptualization.

Declaration of Competing Interest

The authors declare that they have no known competing financial interests or personal relationships that could have appeared to influence the work reported in this paper.

Data availability

Data will be made available on request.

Acknowledgements

This study was carried out within the project "Interdisciplinary approach for the management and conservation of UNESCO World Heritage Site of Historic Cairo - Application to Al-Ashraf Street" supported by Newton-Mosharafa funding programme, a joint fund by the Arts and Humanities Research Council (AHRC) of the UK, Grant No. AH/R00787X/1, and the Science, Technology, and Innovation Funding Authority (STIFA) of Egypt, Grant No. AHRC30799. The authors would also like to acknowledge the support provided by the technical staff of the Structures Laboratories at Imperial College London, particularly Mr. L. Clark, Mr. P. Crudge, and Ms Z. Rydz.

References

[1] D. Losanno, N. Ravichandran, F. Parisi, A. Calabrese, G. Serino, Seismic performance of a low-cost base isolation system for unreinforced brick Masonry buildings in developing countries, Soil Dyn. Earthq. Eng. 141 (2021) 106501.
[2] G. Fortunato, M.F. Funari, P. Lonetti, Survey and seismic vulnerability assessment of the Baptistery of San Giovanni in Tumba (Italy), J. Cult. Herit. 26 (2017) 64–78, https://doi.org/10.1016/j.culher.2017.01.010.
[3] D. D'Ayala, E. Speranza, Definition of collapse mechanisms and seismic vulnerability of historic masonry buildings, Earthq. Spectra 19 (3) (2003) 479–509, https://doi.org/10.1193/1.1599896.
[4] C. Colombo, N. Savalle, A. Mehrotra, M.F. Funari, P.B. Lourenço, Experimental, numerical and analytical investigations of masonry corners: influence of the horizontal pseudo-static load orientation, Constr. Build. Mater. 344 (2022) 127969.
[5] M.F. Funari, B. Pulatsu, S. Szabó, P.B. Lourenço, A solution for the frictional resistance in macro-block limit analysis of non-periodic masonry, in: In Structures, Vol. 43, Elsevier, 2022, September, pp. 847–859.
[6] G. Predari, L. Stefanini, M. Marinković, M. Stepinac, S. Brzev, Adriseismic methodology for expeditious seismic assessment of unreinforced masonry buildings, Buildings 13 (2) (2023) 344.
[7] B. Pradhan, M. Zizzo, V. Sarhosis, L. Cavaleri, Out-of-plane behaviour of unreinforced masonry infill walls: Review of the experimental studies and analysis of the influencing parameters (October), in: In Structures, Vol. 33, Elsevier, 2021, pp. 4387–4406 (October).
[8] A. Moretić, M. Stepinac, P.B. Lourenço, Seismic upgrading of cultural heritage–a case study using an educational building in croatia from the historicism style, Case Stud. Constr. Mater. 17 (2022) e01183.
[9] A.Y. Elghazouli, D.V. Bompa, S.A. Mourad, A. Elyamani, In-plane lateral cyclic behaviour of lime-mortar and clay-brick masonry walls in dry and wet conditions, Bull. Earthq. Eng. 19 (2021) 5525–5563.
[10] D.V. Bompa, A.Y. Elghazouli, Mechanical properties of hydraulic lime mortars and fired clay bricks subjected to dry-wet cycles, Constr. Build. Mater. 303 (2021) 124458.
[11] D.V. Bompa, A.Y. Elghazouli, Shear-compression failure envelopes for clay brick lime mortar masonry under wet and dry conditions, 2021, in: Protection of Historical Constructions: Proceedings of PROHITECH, 4, Springer International Publishing, 2022, pp. 175–185, 2021.
[12] N. Giordano, F. De Luca, A. Sextos, Out-of-plane closed-form solution for the seismic assessment of unreinforced masonry schools in Nepal, Eng. Struct. 203 (2020) 109548.
[13] A.Y. Elghazouli, D.V. Bompa, S.A. Mourad, A. Elyamani, Structural behaviour of clay brick lime mortar masonry walls under lateral cyclic loading in dry and wet conditions (pp), in: Protection of Historical Constructions: Proceedings of PROHITECH, 4, Springer International Publishing, 2022, pp. 164–174 (pp).
[14] A.Y. Elghazouli, D.V. Bompa, S.A. Mourad, A. Elyamani, Seismic performance of heritage clay brick and lime mortar masonry structures. In European Conference on Earthquake Engineering and Seismology (pp, Springer International Publishing, Cham, 2022, pp. 225–244.
[15] N. Trochoutsou, M. Di Benedetti, K. Pilakoutas, M. Guadagnini, In-plane cyclic performance of masonry walls retrofitted with flax textile–reinforced mortar overlays, J. Compos. Constr. 26 (5) (2022) 04022049.
[16] D.V. Bompa, A.Y. Elghazouli, Experimental and numerical assessment of the shear behaviour of lime mortar clay brick masonry triplets, Constr. Build. Mater. 262 (2020) 120571.
[17] M. Deng, Z. Dong, J. Dai, X. Zhao, Out-of-plane strengthening of URM walls using different fiber-reinforced materials, Constr. Build. Mater. 362 (2023) 129597.
[18] F. Parisi, I. Iovinella, A. Balsamo, N. Augenti, A. Prota, In-plane behaviour of tuff masonry strengthened with inorganic matrix–grid composites, Compos. Part B: Eng. 45 (1) (2013) 1657–1666.
[19] X. Wang, C.C. Lam, V.P. Iu, Comparison of different types of TRM composites for strengthening masonry panels, Constr. Build. Mater. 219 (2019) 184–194.
[20] A.K. Thomoglou, T.C. Rousakis, D.V. Achillopoulou, A.I. Karabinis, Ultimate shear strength prediction model for unreinforced masonry retrofitted externally with textile reinforced mortar, Earthq. Struct. 19 (6) (2020) 411–425.
[21] J.A.P.P. Almeida, E.B. Pereira, J.A.O. Barros, Assessment of overlay masonry strengthening system under in-plane monotonic and cyclic loading using the diagonal tensile test, Constr. Build. Mater. 94 (2015) 851–865.
[22] E. Bertolesi, F.G. Carozzi, G. Milani, C. Poggi, Numerical modeling of Fabric reinforced cementitious matrix composites (FRCM) in tension, Constr. Build. Mater. 70 (2014) 531–548.
[23] N. Ismail, J.M. Ingham, Polymer textiles as a retrofit material for masonry walls, Proc. Inst. Civ. Eng. -Struct. Build. 167 (1) (2014) 15–25.
[24] N. Ismail, J.M. Ingham, In-plane and out-of-plane testing of unreinforced masonry walls strengthened using polymer textile reinforced mortar, Eng. Struct. 118 (2016) 167–177.
[25] D.V. Bompa, A.Y. Elghazouli, Drift capacity of textile reinforced mortar masonry walls, SECED 2023 Conf. - Earthq. Eng. Dyn. a Sustain. Future (2023), 14-15 September 2023, Cambridge, UK.
[26] J. Donnini, G. Maracchini, S. Lenci, V. Corinaldesi, E. Quagliarini, TRM reinforced tuff and fired clay brick masonry: experimental and analytical investigation on their in-plane and out-of-plane behavior, Constr. Build. Mater. 272 (2021) 21643.
[27] A. Furtado, H. Rodrigues, A. Arêde, H. Varum, Impact of the textile mesh on the efficiency of TRM strengthening solutions to improve the infill walls out-of-plane behaviour, Appl. Sci. 10 (23) (2020) 8745.
[28] F.A. Kariou, S.P. Triantafyllou, D.A. Bournas, L.N. Koutas, Out-of-plane response of masonry walls strengthened using textile-mortar system, Constr. Build. Mater. 165 (2018) 769–781.
[29] N. Gattesco, I. Boem, Out-of-plane behavior of reinforced masonry walls: Experimental and numerical study, Compos. Part B: Eng. 128 (2017) 39–52.
[30] A.R. Bakkar, A. Elyamani, A.G. El-Attar, D.V. Bompa, A.Y. Elghazouli, S.A. Mourad, Dynamic characterisation of a heritage structure with limited accessibility using ambient vibrations, Buildings 13 (1) (2023) 192.
[31] A. Elyamani, A. Reda, M. Abdel-Hafez, S.A. Mourad, M.M. Hassan, Characterization of construction materials of the historic structures in historic cairo: a case study, Int. J. Conserv. Sci. 14 (2) (2023) 599–616.
[32] Secil Argamassas, Natural hydraulic lime (NHL)—the binder. Available at: 〈https://www.secilargamassas.pt/uploads/documentos/Ficha_Tecnica_NHL_5.pdf〉. Accessed 10 Nov 2019.
[33] C. Ince, M.A. Carter, M.A. Wilson, The water retaining characteristics of lime mortar, Mater. Struct. 48 (2015) 1177–1185.
[34] BS EN 459–2. Building lime: test methods. British Standards Institution, UK.
[35] D.J. Flower, J.G. Sanjayan, Green house gas emissions due to concrete manufacture, Int. J. life Cycle Assess. 12 (2007) 282–288.
[36] Elghazouli, A., Butler, A., Mourad, S., Cheeseman, C., Elyamani, A., 2018. Interdisciplinary approach for the management and conservation of UNESCO World Heritage Site of Historic Cairo. Application to Al-Ashraf Street. UK Research and Innovation, viewed 7 July 2019,
[37] Egernsund Tegl, Chelmer Red Imperial. Available at: https://www.egernsundtegl.com/products/bricks/270-2.2.07-chelmer-red-imperial [accessed 10 November 2019].
[38] CEN (European Committee for Standardization), 2011. EN 771-1:2011. Specification for masonry units Part 1: Clay masonry units. European Committee for Standardisation, Brussels.
[39] Ceresit, 2024. CT325 glass-fibre mesh reinforcing mesh. 〈https://www.ceresit.com/products/facade-solutions/central-pdp.html/ceresit-ct-325/SAP_0201IJC014H2.html〉.
[40] ACI (American Concrete Institute), 2013. ACI 549.6R-20. Guide to design and construction of externally bonded fabric-reinforced cementitious matrix (FRCM) and steel-reinforced grout (SRG) systems for repair and strengthening masonry structures. American Concrete Institute. Farmington Hills, MI.
[41] L. Facconi, F. Minelli, Retrofitting RC infills by a glass fiber mesh reinforced overlay and steel dowels: experimental and numerical study, Constr. Build. Mater. 231 (2020) 117133.
[42] V. Giamundo, G.P. Lignola, A. Prota, G. Manfredi, Nonlinear analyses of adobe masonry walls reinforced with fiberglass mesh, Polymers 6 (2) (2014) 464–478.
[43] CEN (European Committee for Standardization) (2013) EN ISO 13934-1:2013 Textiles. Tensile properties of fabrics. Determination of maximum force and elongation at maximum force using the strip method. European Committee for Standardisation, Brussels.
[44] W. Brameshuber, M. Hinzen, A. Dubey, A. Peled, B. Mobasher, A. Bentur, F. Silva, J. Hegger, T. Gries, J. Wastiels, K. Malaga, Recommendation of RILEM TC 232-TDT: test methods and design of textile reinforced concrete, Mater. Struct. 49 (12) (2016) 4923–4927.

[45] N. Trochoutsou, M. Di Benedetti, K. Pilakoutas, M. Guadagnini, Mechanical characterisation of flax and jute textile-reinforced mortars, Constr. Build. Mater. 271 (2021) 121564.

[46] A. Bilotta, F. Ceroni, E. Nigro, M. Pecce, Experimental tests on FRCM strengthening systems for tuff masonry elements, Constr. Build. Mater. 138 (2017) 114–133, https://doi.org/10.1016/j.conbuildmat.2017.01.124.

[47] P.D. Askouni, C.C.G. Papanicolaou, Role of mortar joints in textile reinforced mortar-to-masonry bond, J. Compos. Constr. 24 (6) (2020) 04020069, https://doi.org/10.1061/(ASCE)CC.1943-5614.0001056.

[48] A.Y. Elghazouli, D.V. Bompa, S.A. Mourad, A. Elyamani, Ultimate in-plane shear behaviour of clay brick masonry elements strengthened with TRM overlays, Bull. Earthq. Eng. 21 (2023) 6273–6315, https://doi.org/10.1007/s10518-023-01775-y.

[49] CEN (European Committee for Standardization), 1999. EN 1052-1:1999 – Methods of test for masonry. Determination of compressive strength. European Committee for Standardisation, Brussels.

[50] ASTM, 2007.ASTM E 519-07, Standard Test Method for Diagonal Tension (Shear) in Masonry Assemblages, ASTM International.

[51] CEN (European Committee for Standardization), 2016. EN 1052-2:2016 – Methods of test for masonry. Determination of flexural strength. European Committee for Standardisation, Brussels.

[52] LaVision - DaVis digital image correlation software ⟨http://www.lavision.de/en/products/davis-software/index.php⟩.

[53] A. Mujdeci, D.V. Bompa, A.Y. Elghazouli, Confinement effects for rubberised concrete in tubular steel cross-sections under combined loading, Arch. Civ. Mech. Eng. 21 (2021) 1–20.

[54] Jesse, F., Schicktanz, K. and Curbach, M., 2009, May. Obtaining characteristic material strength of Textile Reinforced Concrete (TRC) from laboratory tests. In 9th International Symposium on Ferrocement and Thin Reinforced Cement Composites (Ferro-9) (pp. 18-20).

[55] D.V. Bompa, A.Y. Elghazouli, Compressive behaviour of fired-clay brick and lime mortar masonry components in dry and wet conditions, Mater. Struct. 53 (3) (2020) 60.

[56] CEN (European Committee for Standardization), 2016. EN 772–1:2011 Methods of test for Masonry Units - Part 1: Determination of Compressive Strength. European Committee for Standardisation, Brussels.

[57] CNR(Advisory Committee on Technical Recommendations for Construction), 2018. CNR-DT 215/2018 guide for the design and construction of fibre reinforced inorganic matrix systems for strengthening existing structures. Rome.

[58] CEN (European Committee for Standardization), 2005. EN 1996-1-1: 2005 Eurocode 6: design of masonry structures—general rules for reinforced and unreinforced masonry structures. European Committee for Standardisation, Brussels.

[59] A. Prota, G. Marcari, G. Fabbrocino, G. Manfredi, C. Aldea, Experimental in-plane behavior of tuff masonry strengthened with cementitious matrix–grid composites, J. Compos. Constr. 10 (3) (2006) 223–233, https://doi.org/10.1061/(ASCE)1090-0268(2006)10:3(223).

[60] A. Bellini, A. Incerti, M. Bovo, C. Mazzotti, Effectiveness of FRCM reinforcement applied to masonry walls subject to axial force and out-of-plane loads evaluated by experimental and numerical studies, Int. J. Archit. Herit. 12 (3) (2018) 376–394.

[61] A. Bellini, A. Incerti, C. Mazzotti, Out-of-plane strengthening of masonry walls with FRCM composite materials, Key Eng. Mater. 747 (2017) 158–165.

[62] CEN (European Committee for Standardization), 2021. EN 1998-3: 2021: Eurocode 8. Design of structures for earthquake resistance — Part 3: Assessment and Retrofitting of Buildings and Bridges. European Committee for Standardisation, Brussels.

[63] H. Kupfer, H.K. Hilsdorf, H. Rusch, Behavior of concrete under biaxial stresses, Acids J. Proc. 66 (8) (1969) 656–666.